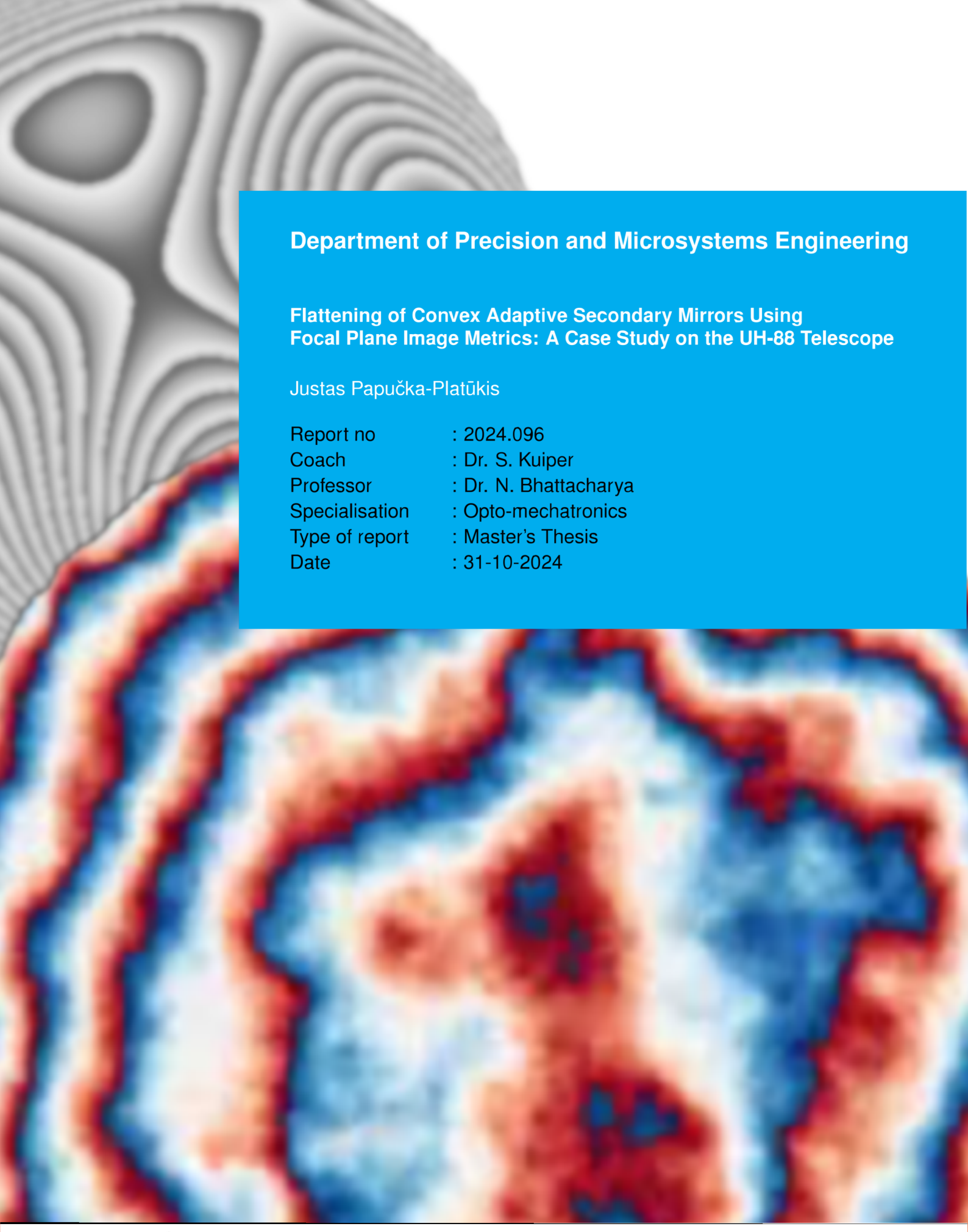

Department of Precision and Microsystems Engineering

Flattening of Convex Adaptive Secondary Mirrors Using Focal Plane Image Metrics: A Case Study on the UH-88 Telescope

Justas Papučka-Platūkis

Report no : 2024.096
Coach : Dr. S. Kuiper
Professor : Dr. N. Bhattacharya
Specialisation : Opto-mechatronics
Type of report : Master's Thesis
Date : 31-10-2024

Delft University of Technology

High-Tech Engineering Master thesis

Flattening of Convex Adaptive Secondary Mirrors Using Focal Plane Image Metrics: A Case Study on the UH-88 Telescope

Authors:
Justas Papučka-Platūkis (5630223)

Supervisors:
Dr. S. Kuiper
Dr. N. Bhattacharya

November 1, 2024

Abstract

Adaptive optics (AO) are essential in ground-based telescopes to correct atmospheric distortions and achieve high-resolution imaging; adaptive secondary mirrors (ASMs) integrate deformable mirrors directly into telescope optics but typically require a wavefront sensor (WFS) for calibration and flattening. When a WFS is unavailable or nonfunctional, alternative methods are needed. This thesis explores the feasibility of flattening the convex ASM of the UH-88 telescope without a WFS, using only a natural guide star and focal plane imaging. By developing a numerical model of the UH-88 system—including the deformable mirror, Mauna Kea atmospheric aberrations, and focal plane camera characteristics—we employed an image metric based on the second moment of intensity to evaluate image quality, adjusting Zernike mode coefficients via the Nelder-Mead simplex optimization algorithm to control mirror shape. Experimental validation using a laboratory setup that replicated key aspects of the UH-88 system confirmed that the ASM could be flattened to within 100 nm RMS surface error, meeting passive mirror operation requirements. The flattening was achieved within a 10-minute timeframe using only focal plane images of a natural guide star distorted by atmospheric turbulence. This study demonstrates that flattening a convex ASM without a WFS is feasible using focal plane image metric optimization, offering a practical solution when the WFS is unavailable or calibrated commands are outdated, thereby ensuring continued high-quality telescope operation.

Contents

Introduction

The main challenge for contemporary advanced ground telescope systems is to correct the light distortion created by differences in refraction index within the atmosphere. In attempts to improve image quality, adaptive optics (AO) has been the dominant practice. A fully functional AO system will have deformable mirrors (DM) and a wavefront sensor (WFS). The technology has advanced significantly and DMs are no longer a separate instrument of the telescope but have been integrated as adaptive secondary mirrors (ASM) allowing for corrected light to reach any other instrument [1]. Although there is now quite a few telescopes with ASM, there are still many challenges to tackle when implementing ASM. Particularly the research will focus on the UH-88 convex ASM implementation case. Further chapters will explain the complexity of the system, its potential pitfalls, and proposals to make the system more robust.

0.1 Working principle of AO

The purpose of AO is to correct wavefront aberrations, which are parameterized by the wavelength-dependent phase difference from the flat wavefront, as illustrated in Figure 1a. An uncorrected aberrated wavefront results in image blurring. For telescopes, the distortion occurs due to the turbulent airflow in the atmosphere with an uneven refraction index. The working principle of a DM is shown in Figure 1b. It involves deforming the continuous mirror sheet with the aid of actuators, thereby altering the phase of the wavefront. This change corrects the phase of the incoming wavefront restoring the reference wavefront to produce a diffraction-limited image. While there are various types of actuation and realizations of non-continuous deformable surfaces, all ASMs feature continuous surfaces actuated by electromagnetic actuators. The UH-88 ASM uses hybrid variable reluctance (HVR) actuators[2], in contrast to the voice-coil type actuators employed by the LBT, Magellan, MMT, and VLT. The advantage of HVR actuators is that they do not require active cooling, allowing for a higher density of actuators [3].

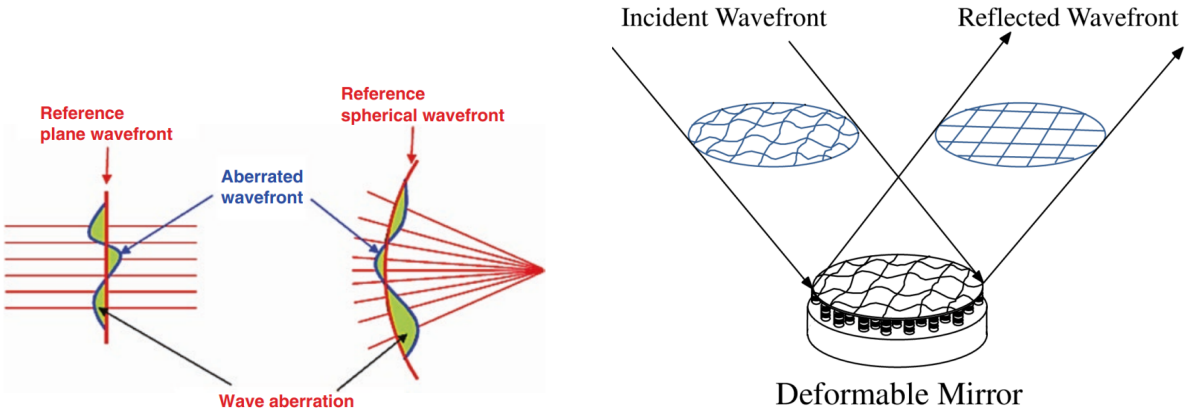

(a) Wavefront aberration [4]

(b) Wavefront corrector[5]

Figure 1: Working principle of the DM

To effectively operate the DM, both a controller and a wavefront sensor (WFS), are required. The general control scheme is depicted in Figure 2. For telescopes, the incoming aberrated wavefront combines atmospheric distortion with mirror surface error (SFE). The aberration is measured by the WFS, which then generates a control signal to counteract the aberration. This closed-loop operates to maintain an aberration-free image. In such systems, non-common path (NCPA) error is inevitable, due to the different paths from the beam splitter

to the WFS and the camera. Notably, in most microscopy cases, it is not possible to measure the wavefront directly [6]; observation is only possible with the camera. The absence of a WFS in microscopy systems means that wavefront correction is not affected by NCPA error.

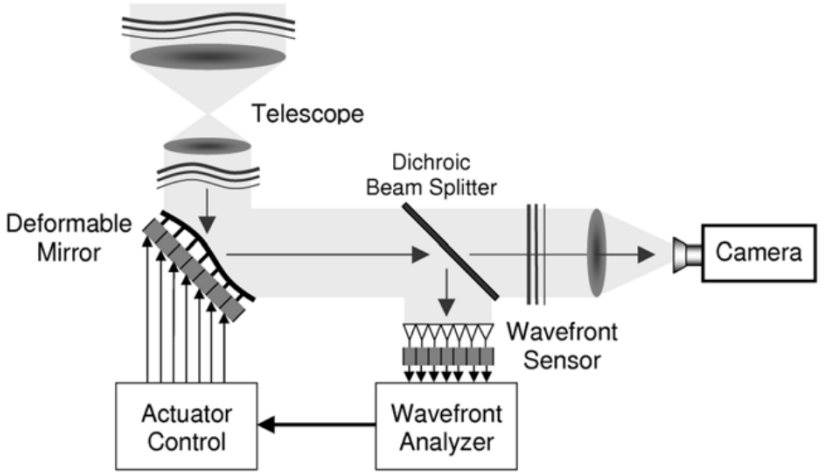

Figure 2: General scheme of adaptive optics system components [7]

0.2 Wavefront sensor

The typical phase variation for visible light is on the scale of nanometers. The time it takes for light to travel such a distance is on the scale of 10e-17 seconds, making it impossible to directly measure the phase difference. The only way to measure wavefront aberrations is through light intensity measurement. The most widely used method is the Shack-Hartmann sensor, which samples the wavefront using a matrix of tiny lenses. An example of a single lenslet is shown in Figure 3, measuring the local slope of the wavefront[8]. By combining these local slope measurements, the full wavefront can be recreated. Although this sensor is effective at measuring high-order wavefront deformations, its observable range is limited. This limitation officially termed the dynamic range, is determined by the lenslet diameter, its focal length, and the dedicated sensor area. Once the spot leaves the area, it is no longer detectable, meaning that the steeper slope becomes invisible. Thus, relying on the wavefront sensor as the only measurement tool is not always possible. Especially when the telescope is at the start of operation and is not yet in the wavefront range.

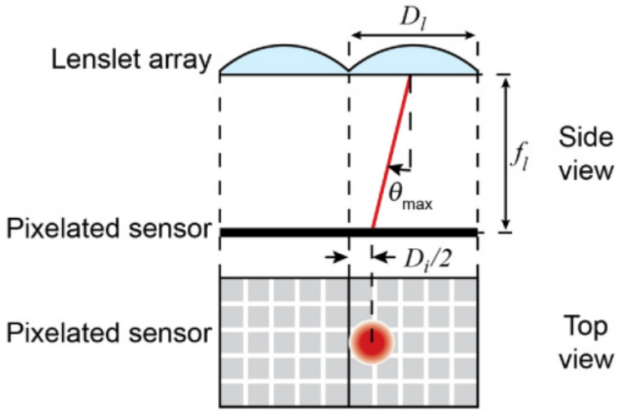

Figure 3: Principle of Shack-Hartmann wavefront observation [8]

0.3 Convex ASM and lack of WFS

It can be a choke point for the entire system if either WFS or ASM cannot perform as intended. This kind of example has been shown with Magellan ASM [9] [10], where the uncalibrated mirror is out of the range of the

WFS. Without the ability to know the mirror's shape, it is impossible to flatten it. Therefore, there is a clear need for a life-boat method that would be capable of bringing the mirror shape back into the wavefront range to enable a full control loop.

Even if it is not possible to directly measure the wavefront, the focal plane image of the star taken with a photosensitive array device, such as a CCD camera still contains information about the wavefront shape. This light point source in the object plane after passing through the optical system ideally converges to a single point in the image plane. It is spread over a small area due to diffraction and is called a point spread function (PSF). The image produced by the camera can be evaluated to determine whether the ASM is in its optimal shape. This evaluated image is then used to guide the optimization algorithm which controls the mirror shape. Because camera-based observation does not have any direct information about the wavefront shape, it is impossible to correct the mirror shape in a single command. Thus the problem becomes a black box and the first basic step in enabling the control of the mirror is to use a direct search optimization algorithm. In an attempt to find the intended mirror shape, it takes the measure of image quality and issues a new shape that is supposed to improve the mirror shape and thus the image. This process continues until the time limit or the optimum is reached. Therefore the method has the name of image metric based optimization.

The flatness goal which would be considered sufficient will be 100 nm RMS mirror surface error. The figure was taken as an approximation from the development paper of UH-88 ASM which indicates the requirement of 80 nm for flattening with pre-calibrated commands [2]. This problem leads to the first part of the research question:

> Can a deformable mirror be flattened to 100 nm RMS SFE while being controlled by focal plane image metric based optimization?

The other issue is with the wavefront of the light source used for the observation. When observing a natural star, the light wavefront is distorted by the atmosphere and additionally by un-actuated DM. Thus it would be ideal to isolate the DM surface error from the atmosphere such that it could flatten perfectly. To achieve this the light point source could be put within the optical system to simulate the star without the aberration, as was done for the Magellan ASM calibration. Unfortunately, this is rather impossible when the ASM is convex rather than concave, as is the case for UH-88 ASM. The focal point of the convex mirror is behind its reflective surface; thus, it is impossible to introduce an artificial light source within the optical system. This leaves the only economical option to observe a natural guide star. It means that the observed point source will be distorted by the atmosphere. This leads to the second part of the research question:

> Can a DM be flattened using only a natural guide star with a distorted wavefront?

Because the only available light source is a natural star it means that the amount of light arriving at the camera will be very low and will require long exposure to have a sufficient signal-to-noise ratio. The exposure time influences the total flattening method time as it will require multiple images to achieve a good mirror shape. Since the telescope exploitation time is expensive there is a 10-minute time limit imposed for the entire flattening procedure. This limit was proposed by the director of UH-88 Mark Chun. This leads to the final part of the research question?

> Can a DM be flattened within 10 minutes?

0.4 Research approach: Requirements, Modeling, and Testing

To answer the research questions and validate the flattening method a numerical model of the UH-88 system's most critical components will be coded. To use the model for method evaluation and make it relevant to the UH-88 system, the requirements for its components will have to be determined first. These parameters stem from a detailed analysis of the most important parts of the UH-88 system. This involves the light source, atmosphere, ASM, and available camera. Further, the test setup will be built to validate the method and determine the discrepancies from the model. It will follow the same requirements to match the model and enable comparison as closely as possible.

Requirements

The main components of the system here will be the deformable mirror, the light source, and most importantly the camera. The only possible light source for a system with convex ASM is the star of the night sky. First, this

means that the intensity of light is limited; second, the light is distorted due to the atmosphere, which results in a wider distribution of PSF. The signal generated within the sensor is distorted by device-specific noise and depends on the signal-to-noise (SNR) ratio. With short exposure, the light will not generate a strong signal and will result in a noisy image. An image where it is difficult to distinguish between actual light and noise cannot be interpreted to determine the quality of the PSF shape. Thus the integration time has to be long to increase the signal-to-noise ratio.

Modeling

A numerical model will be used to evaluate the feasibility of the image metric-based optimization of mirror shape. The simulation of the system will help in identifying the capabilities of different system components. The model is based on the Python package for high-contrast imaging (HCIPY) simulations[11]. The model will contain previously mentioned components in light wavefront propagation order. Light source wavefront with defined power with the size of UH-88 telescope aperture; atmospheric multi-layer model for Mauna Kea station; additional random wavefront distortion to simulate initial mirror shape; camera module with defined pixel size and noise level. The compositions of these modules enable an accurate simulation of the UH-88 system. The Nelder-Mead simplex optimization algorithm is taken from the SciPy library.

Test setup

Following the requirements for the model, the test setup is built to be able to validate the method. It is not possible to replicate the system, for example, the available camera for testing is CMOS with much more noise compared to the electron-multiplying CCD (EMCCD) available in UH-88. To compensate for the difference signal can be increased to achieve a better match of the EMCCD SNR ratio. The DM available for the test is also not convex, but rather flat, thus the optical system is built differently than the Mauna Kea telescope. The Roddier wavefront curvature measurement method will be used to evaluate the contributions of wavefront distortion within the test setup. It will provide more insight and credibility when evaluating the final results of the test.

Chapter 1

Requirements

To answer the research question the flattening method based on image metric optimization will be used. To be a viable control method for UH-88 it has to follow requirements that would stem from the the environment and characteristics of UH-88. After the method is modeled and later validated with the test setup, it will be determined whether the method will be applicable to the UH-88 telescope.

The validation criteria for the flattening method are determined by further analysis of the sub-questions and UH-88 characteristic comparison with the test setup. The evaluation and comparison between available test instruments and UH-88 will set the threshold requirements for validation criteria. However, many important aspects of the optical system will affect the focal image-based control, only the most crucial will be considered. These important aspects of the system are: the available imaging instrument, the optical system, and the light source characteristics. The further sub-questions are related to these parts of the system and lead to requirements for the method.

- When is the mirror flat? $\Longrightarrow$ Required passive flatness, number of modes to control.
- What instrument is available for observation? $\Longrightarrow$ Camera parameters, noise sources.
- How strong the light of the star is? $\Longrightarrow$ Magnitude of the light source in W/m^2.
- What are the sources of error? $\Longrightarrow$ The biggest contributors of error and their sufficiency for the model.
- How much time does the method have to converge? $\Longrightarrow$ Convergence time limit, the time scale of the algorithm.

This chapter provides an overview of UH-88 and its comparison to available testing instruments. The detailed answers to the questions and subsequent requirements will eventually become validation criteria for the chosen method's applicability to the UH-88 ASM.

1.1 Flattening figure

The initial surface error heavily influences the final flatness as not all aberrations can be corrected. The flattening here is meant not in a literal sense, but to have the surface of the mirror close to the ideal intended shape. The initial surface error will be compared between planned ASM parameters and test DM for modeling purposes, to determine possible implications for the final figure when determining the validity of the method. Further, it is required to determine the observation instrument parameters and how they compare to the available cameras. Because the wavefront sensor is not available for testing a method using only a CCD detector for evaluating performance will discussed. The final important part is that the extended scene of the night sky has to be modeled and simulated in the test setup such that it does not invalidate the results. Thus it will be discussed how to approach such a problem.

1.1.1 Initial and final passive flatness figure

The first and most important is the mirror flatness figure at which the optical system is considered operational, this will also serve as a target figure for the validation of the method. The spatial order of SFE is separated into high, mid, and low. The mirror surface is manufactured to ensure that the high-order spatial errors are eliminated [12], as these errors when located between the actuators become uncorrectable. Thus the surface

error of lower orders is not as crucial to eliminate. Additionally, the UH-88 has a separate focusing stage and tip/tilt correction from RoboAO module[13]. Piston, tip, and tilt modes will be corrected during initial alignment. The final SFE requirement for the mirror before any correction is 6000 nm PV or 630 nm RMS which is 2λ for WFE due to the reflection. Together with thermal deformation and gravity sag the full RMS error is expected to increase to 690 nm. After closing AO loop the remaining error is 21 nm RMS. The remaining SFE of the DM1 is of similar magnitude [14]. The Table 1.1[3][14][15][16] presents a detailed comparison of

Table 1.1: Comparison of DM and ASM parameters

	DM1	**DM3**	**Flash**	**UH-88 ASM**
Mirror diameter (mm)	150	150	150	620
Facesheet thickness (mm)	1	1	3.3	3.5
Facesheet form	flat	flat	flat	convex aspherical
Initial SFE (μm PV)	8	15.5	5.3	6
Number of actuators	57	57	18	210
Actuator spacing (mm)	18	18	39	39
Free stroke (μm)	40	40	34–40	35
Inter-actuator (μm)	10	10	5	4
Actuator constant (nm/mA)		39.6	46.5	
Resolution (surface, nm)				0.5
Linearity (%)	99.5	99.4	95.2	99.5
Hysteresis (avg for 20–120 mA, %)		2.1	1.8	
Actuator coupling (%)	40	37	34.2	35
Power dissipation for flattening (W)	0.2	0.189	0.007	3
Best flat (nm RMS)	30	28	15	23
Bandwidth (Hz)	100	100	150	100

different deformable mirrors which in principle share the same actuators, layout, comparable size and are all manufactured by TNO. The ASM for UH-88 is still in development thus the figures are estimates for the final result. The test for the algorithm will be performed with DM 1 which is essentially the same as DM3 and has similar initial SFE and final flatness to UH-88 ASM. Thus it has the same range for the algorithm to correct and validate. Because the mirror will be controlled by Zernike modes, the number of actuators does not influence the algorithm search space. Although there will be differences in how well the positions of the actuators fit the Zernike modes. The discrepancy between applied and measured shape was observed with the DM3 [3], where it seems that the defocus and higher order spherical aberration modes were not controlled as well as others, presented in Figure 1.1. However, the paper did not present how the Reduced χ^2 values were calculated which made it difficult to interpret how large is the actual discrepancy between the applied and controlled modes. This might pose a challenge in reaching the determined final flatness and other modes like Karhunen-Loeve or mirror modes which might have better fit to the hexagonal pattern of the actuators.

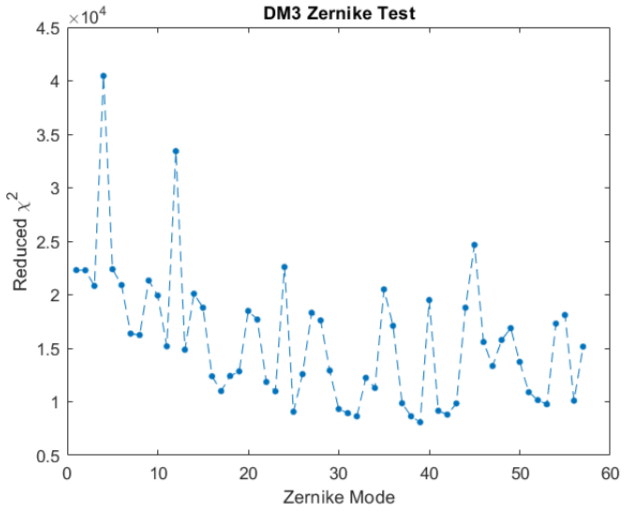

Figure 1.1: Reduced χ^2 values for individual Zernike modes applied to the mirror.

The requirement for final surface error after flattening command with precalibrated IM is set to be $\lambda/8$ at a wavelength of 630 nm which equals 80 nm [2]. However in this case it is considered that the IM and LUT are in a state that does not satisfy this figure. Thus it is not unreasonable to set the requirement for the DM1 to be at 100 nm which is still within the range of the wavefront sensor. To determine how the model and test satisfy this measure will be discussed within respective chapters.

1.1.2 Error sources affecting flatness

The thermal variation in surrounding air will result in distortion due to different coefficients of thermal expansion (CTE) of the system. During finite element (FEM) analysis it was determined that it results mostly in focus aberrations. This is because the actuator struts only constrain the motion of the mirror along the optical axis. This aberration can be removed with the focusing stage with the remaining error of 3 nm RMS[2]. Therefore the error will not be considered for modelling.

FEM analysis of gravity sag along the optical axis resulted in distinct trefoil aberration. Correctable SFE of 280 nm RMS with residual uncorrectable SFE of 1 nm RMS. Gravity sag perpendicular to the optical axis resulted in a correctable error of 136 nm RMS, twice as low with a residual of 3 nm RMS [2]. Although the error seems large, the calibrated values for different positions will correct the error. The error will not be considered within the model.

The print-through error results from the actuator strut stressing the mirror surface. The stress can be caused by gravity sag, bonding shrinkage, and CTE difference. The total summed SFE is expected to be 6.9 nm RMS[2]. The magnitude of this error is an order lower than the set target and will not be considered for modeling. Although it will be present in the test it is not expected to be significant for the performance of the chosen method.

The discussed errors are presented in Table 1.2. The green color marks the error to be modeled, the red color marks the errors that are insignificant and will not be modeled. Modelling of the gravity sag will not have a great effect, as it can be seen the contribution to the cumulative error is only 32 nm. This particular error is also compensated by a calibrated look-up table.

Table 1.2: Different error sources, their magnitudes and contribution to cumulative error

	Group	**Order**	**WF error (nm RMS)**	**Cumulative error (nm RMS)**
Manufacturing SFE	10000-1000	Low-Mid	1200	1200
Gravity sag	1000-100	Low	280	1232
Thermal distortion	100-10	Low	78	1235
Thermal convection	10-1	High	10	1235
Actuator print through	10-1	High	7	1235
Non-linearity	10-1	Low	5	1235

1.2 Focal plane detector

The output of the system is observed with the focal plane detector and is considered the only available tool for measurement. The focal plane detector for the UH-88 flattening method will be iXon ultra 888 electron-multiplying CCD (EMCCD) manufactured by Andor. The detector is part of the adaptive optics module Robo-AO-2. The camera available for testing is BFS-U3-123S6M-C with a SONY IMX253 CMOS sensor. Notably, the CMOS sensors have much more noise than CCD cameras and have lower quantum efficiency (QE) which is evident in Table 1.3.

Table 1.3: Comparison of UH-88 and test setup sensors

Detector	**Type**	**Format**	**Pixel size (um)**	**Pixel scale (arcsec)**	**Read noise (e-)**	**Frame rate (Hz)**	**QE (%)**	**Dark current (e-/pix/sec)**
iXon Ultra 888	EMCCD	1024^2	13.00	0.03	<1	26	90	0.00025
Sony IMX253	CMOS	4096x3000	3.45	1.587	2.18	30	65	2.99

Photon noise

The test camera QE is 30% lower than the EMCCD; thus, fewer photons are converted to measurable signals. This directly translates to the intensity of the light source requirement being 30% more to compensate for the lack of QE. The signal is dependent on quantum noise is calculated with Equation 1.1[17] and is proportional to the P photon flux which is the number of photons per pixel per second and integration time. Thus to match the signal received by the EMCCD camera either integration time has to be increased or the photon flux. The integration time will affect the smearing created by the atmospheric aberrations. To leave this parameter independent for testing how well the algorithm performs in different integration times, only the photon flux should be changed.

$$S = P \cdot t \cdot QE \tag{1.1}$$

Dark noise and read noise

The dark noise presented in Equation 1.2[17] which is electron count per pixel per second, depends only on dark current and integration time. This noise is significantly larger with the IMX253 sensor compared to UH-88 and will be limiting noise with long exposures, but cooling the sensor below zero could mitigate this error and will be implemented if necessary. The read noise in general is caused by different electronic noise, in CCD it is caused by an output amplifier. It is measured electrons per pixel per readout, and for the EMCCD camera, it is below single electron due to electron multiplication [18]. The CMOS camera has a 2.13 electron RMS error per pixel per readout. This error is more evident where the mirror is severely deformed and does not form a perfect point spread function. The total photon flux in the aperture is then distributed over a large area and can be on the same magnitude or close to the read-out noise. Whereas when it is concentrated in a small area the signal becomes strong and the contrast with the readout noise increases such that it becomes insignificant. Thus at low integration times or where with large WFE, the read-out noise will be prevalent and might interfere with the image metric performance. If this proves to be a limiting factor in low light conditions, binning the pixel would increase the photon count, and decrease the number of effective pixels and thus the readout noise. The only noise dependent on the intensity of the light is photon noise and thus increased intensity should not affect other noise sources.

$$S = \sqrt{I_d \cdot t} \tag{1.2}$$

Pixel scale and light source size

The pixel scale here is the subtended angle of the sky for the single pixel. The scale and the apparent size of the objects in the sky depend on the telescope's optics as it is only a relation between the field of view and the pixel count of their size. The brightest star appearing in the night sky is Sirius A with an angular diameter of 6.048 mas at 694.1 nm. The pixel scale for EMCCD of UH-88 is 30 mas/pix, thus without diffraction and aberrations the star would appear on a single pixel. Therefore the final image will be determined by the diffraction of the optics rather than the pixel scale.

A simple approximation of the airy disk diameter is determined by Rayleigh criterion Equation 1.3[19] expressed in linear resolution rather than angle in radian due to small angle approximation. The wavelength of $590nm$ is chosen for evaluation, as this was a readily available narrow-band LED for the test setup. With a focal ratio of 10 for UH-88 the airy disk diameter results in $14.4\mu m$ and for the test setup almost twice as small $8.4\mu m$, due to it having the focal ratio half of the UH-88. This is due to the diffraction disk diameter being inversely proportional to the diameter of the optics. Notably, the diffraction of the UH-88 falls just outside of a single $13\mu m$ pixel, whereas the airy disk for the test is registered by 2.4 pixels of $3.45\mu m$ size.

$$\Delta l \approx 2.44 \cdot \frac{\lambda \cdot f}{D} \Rightarrow \Delta l \approx 2.44 \cdot \lambda \cdot f/\# \tag{1.3}$$

The available pinhole diameter for the test was $5 \pm 1\mu m$ which is well within the diffraction limit. This can be seen in the Figure 1.2, where the FWHM of the focal point of the secondary reflection is captured just outside of 2 pixels. To match the UH-88 observational capabilities in the test it's required to use pixel binning such that the point source is captured within 1.1 pixels. Therefore the sensor will use 2x2 pixel binning which results in an airy disk being captured by 1.063 pixels. Compared to using binning of 3x3 would result in 0.81 pixels, which is still relatively close to 1 pixel. In this case, it would have a significant 33% less resolution and might affect the final quality of algorithm convergence. Binning reduces pixel number by half and thus the readout error as it is dependent only on pixel number.

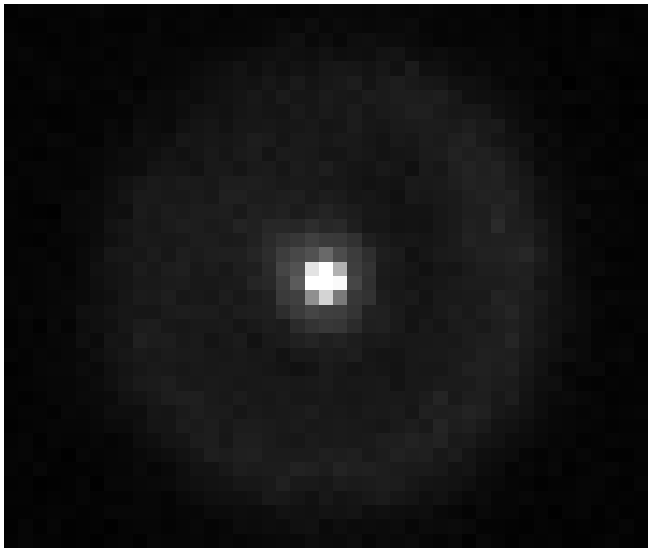

Figure 1.2: Optical setup secondary reflection focal point

1.3 Light source intensity

Having defined the size of the light source it is important to determine the matching intensity of the light coming from a star or simply a point source for the test setup. To determine the quality of the image, the metric uses intensity values registered by the sensor which are direct result of photons generating electric charge within it. If the perceived intensity with the sensor, within the model and the test, is lower or higher than in reality, respectfully this would result in either dismissing the perfectly capable method or overestimating the capability of a worthless method. Covered in the previous chapter were various noise sources plaguing the measurement, which were measured in electrons. The signal level within a sensor is dependent on the energy per wavelength per area per second, namely spectral irradiance ($watt/m^3$). The radiant flux here is measured in watts which is joules per second, the area is square meters, and the wavelength is in meters. The signal is subject to power losses due to absorption in the atmosphere and most notably the various noises of the sensor.

An important note is that the light from the star is incoherent and wideband, where different wavelengths contain different energy. To receive a strong signal it is required to capture a wide spectrum of light, meaning it has to be integrated over the spectrum. Although there is a large difference in the appearance of a point source due to the diffraction of narrowband light. The image over the wideband would not have a clear interference pattern when compared to narrowband filtered light. But for simplicity of modeling and test setup, there will be a single wavelength considered, the exact reason will be covered in the modeling part.

Sensor quantum efficiency

To simulate the total power observed by a monochromatic sensor it will have to be integrated over wavelength bandwidth. This band will be defined by the highest quantum efficiency range of the sensor. The QE change over the spectrum for both sensors IMX253 and iXon ultra 888 is presented in Figure 1.3. Both sensors are roughly centered around the V-band (551nm)[20], and will have the highest QE $\pm 100nm$ around it, resulting in a bandwidth of 200 nm. The average QE for the specified bandwidth of IMX253 is 63% and for iXon ultra 888 is 87% (red line).

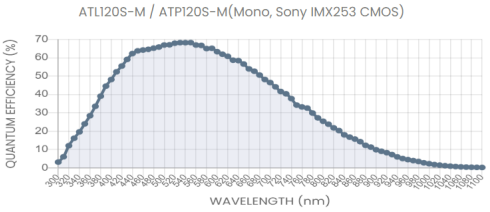

(a) QE curve for IMX253 CMOS sensor[21]

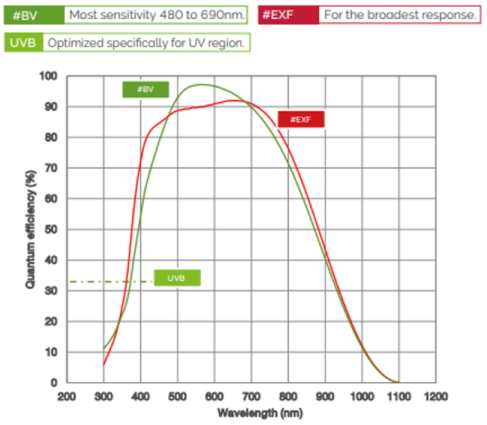

(b) QE curve for iXon Ultra 888[18]

Figure 1.3: QE curves over wavelength for UH-88 and test setup sensors

Star magnitude

For a rough estimate the spectral irradiance (SPI) at the earth's upper atmosphere was taken from [22], and presented in Figure 1.4. The SPI was calculated assuming that the star radiates as a black body, thus using the Planck law to determine the spectral radiance. The Sirius A for the chosen bandwidth is the brightest star between 450 nm and 650 nm. By recreating the polynomial from the graph and integrating over the specified range the irradiance is $3.62e{-}5 W/m^2$. Multiplying it by the area of the pupil with a diameter of 2.2 m the radiant flux was $1.4e{-}4 W$. The light passing through the atmosphere will result in scattering and absorption, ideally, these values should be applied to spectral irradiance to better simulate the total energy. But for simplicity, it assumed that only 20% of determined power will reach the earth's surface.

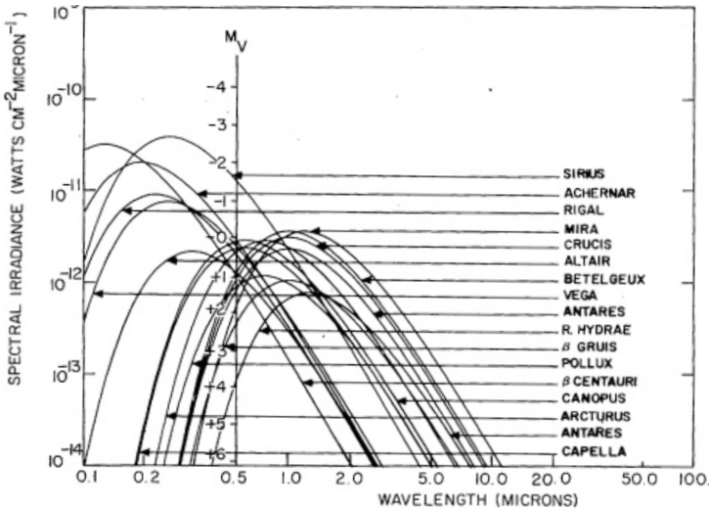

Figure 1.4: Spectral irradiance of brightest stars at the upper atmosphere

The Table 1.4 is presented to summarize the changes to the test setup camera and compare it to the UH-88 optics and sensor. The photon flux compensation is due to the test sensor having a 27% smaller quantum efficiency. Potentially the photon flux can be increased further to simulate the electron multiplication of the UH-88 sensor to match the Signal to Noise ratio and combat the dark current noise.

Table 1.4: Test setup sensor and optical parameters with 2x2 pixel binning[23]

	Resolution (pix)	**Pixel size (um)**	**Focal ratio**	**Pupil diameter (m)**	**Airy disk diameter (um)**	**Point source size (pix)**	**Photon flux compensation**
UH-88	1024x1024	13	10	2.2	14.4	1.1	100%
Test setup	2048x1500	7.9	5.9	0.152	8.4	1.063	127%

1.4 Algorithm convergence time

The control of the mirror is done by multiple evaluations within the optimization algorithm. For determining the convergence of the algorithm, it utilizes a comparison between past results. The result here is generated by the image metric and sufficient power level is required to achieve success. A sufficient integration time is required to reach the desired signal power. Thus the total optimization time directly scales with the integration time of each frame. The time limit of 10 minutes for algorithm convergence was suggested in a personal conversation with the astronomer of UH-88, Mark Chun. To fit between sufficient signal power and convergence time, it is necessary to determine the optimal integration time.

Time-sensitive limiting factors for the algorithm convergence will be atmospheric aberrations and sensor noise. The camera noise will be most prevalent at weak signal power and will introduce large variations in determining the quality of the PSF. To decrease the error signal has to increase, meaning longer integration time. Regarding the atmosphere, the dynamics are on the order of single microseconds[24]. Due to the WF variations over the integration time, the image becomes blurry and smeared. If the integration time is too short, the smearing will not be uniform between the frames and will cause convergence issues. If the frame exposure time is too long it will not be able to converge within the time limit. Therefore it is necessary to find the optimal time where the algorithm convergence is robust, but also short that it fits within the time limit.

It is not possible to determine the analytical relation between atmospheric aberrations, camera noise, and image metric evaluation. The only option to find such a relation is the numerical modeling of each part. To begin to understand such evaluation, an overview of these model parts is necessary. Therefore the detailed analysis of image metric performance will be covered in further chapters of the model section.

Chapter 2

System modeling, method verification

The further chapter details the numerical model for a mirror shaping method using Fourier optics and adaptive optics control to correct system aberrations. Emphasizing the Fourier transform's role in modeling wavefronts and PSF, the model considers essential system components, including sensor noise, atmospheric aberrations, and mirror surface errors (SFE). This multi-faceted approach integrates Zernike modes to control the deformable mirror (DM) and assesses image quality through the second moment of intensity, while optimization uses the Nelder-Mead algorithm. The results demonstrate that the model achieves the desired 100 nm RMS wavefront error correction, with practical performance limits and considerations for future implementation on the UH-88 system.

2.1 Modeled parts of the system

2.1.1 System optics

The Fourier optics is one of the most common ways of modeling wave optics. It is fundamentally different from ray-tracing which treats the light as a bundle of rays. Although it is much faster than Fourier optics, it is not possible to model interference with the ray-tracing and thus it is more suited to model wavefronts and its corresponding PSF. The basic mathematical relation between complex pupil function and PSF is shown in the Figure 2.1[25].

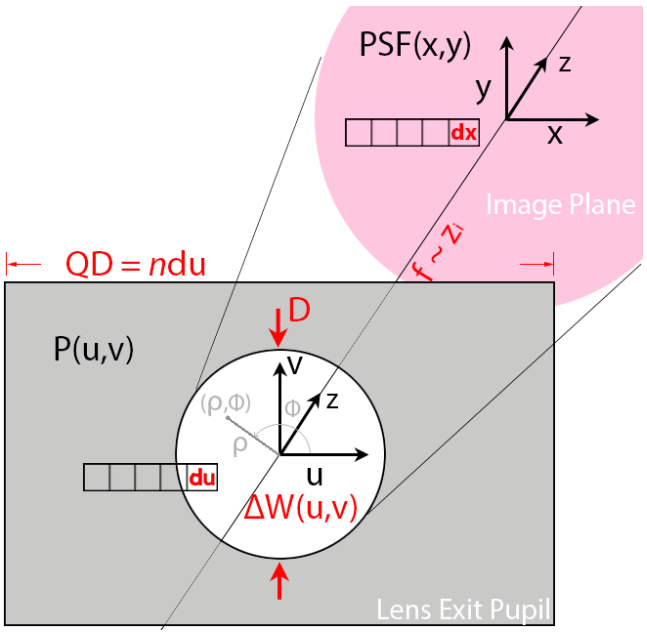

Figure 2.1: Complex pupil function relation to the PSF

The complex pupil function is presented in Equation 2.1[26], where $P(u, v)$ represents the transmission function of the pupil and its plot is presented in Figure 2.2a. Notably, this is not an actual UH-88 pupil, but

only a size equivalent pupil without obstruction. As the first front for testing, it was chosen to make a basic case of the telescope model.

$$\mathcal{P}(u,v) = P(u,v) \odot e^{i\frac{2\pi}{\lambda}\Delta W(u,v)} \tag{2.1}$$

The $\odot$ sign represents element-wise multiplication with the complex expression of wavefront aberration function $\Delta W(u,v)$. The latter function holds the phase difference in the unitary distance at each coordinate location. To convert it to a specific wavelength in radians it's required to multiply the whole wavefront by $\frac{2\pi}{\lambda}$. The full complex pupil equation can then be Fourier-transformed (FT) and with squared modulus taken the result will become a point spread function, presented in Equation 2.2 [26]

$$PSF(x,y) \propto |\mathcal{F}[\mathcal{P}(u,v)]|^2 \tag{2.2}$$

In the case of a flat wavefront, there is no aberration and the complex function becomes 1 and there is only the transmittance pupil function remaining. Such a case represents perfect optics and a resulting PSF will be diffraction-limited. The resulting PSF of the perfect UH-88 aperture-sized pupil plane onto the detector with $13\mu m$ pixels is presented in Figure 2.2b. The HCIPy package used here shifts the plotting grid such that the zero position is in the center of the central pixel. The PSF is slightly larger than an approximation with Equation 1.3, but such precision can be considered sufficient for modeling.

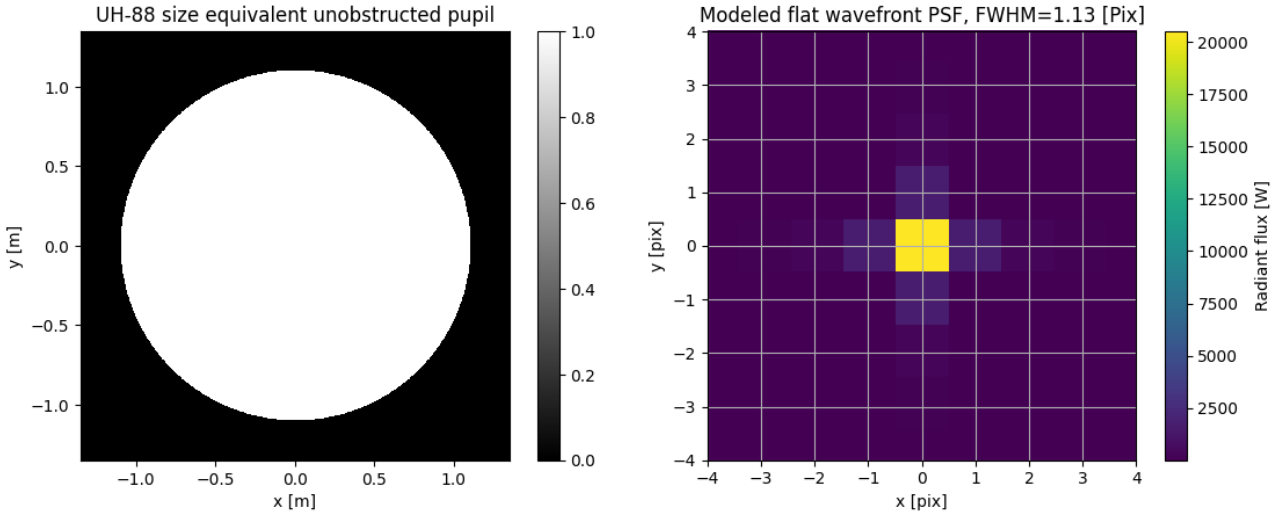

(a) 2.2 meters diameter unobstructed pupil

(b) Modeled flat wavefront diffraction PSF

Figure 2.2: Pupil and focal planes before and after Fourier transform

Thus, an important conclusion is that a single Fourier transform is required to model a single wavelength wavefront PSF. To model a wideband light, for example, white light, multiple Fourier transformations of a range of wavelength wavefronts are necessary, and then their corresponding PSF are added together. A single Fourier transform of a wavefront takes roughly 1 second, and it's expected to perform hundreds of WF evaluations for the optimization. Thus the evaluation time grows with a coefficient of the number of FTs performed. The choice was made to use a single wavefront wavelength, but to use the total energy of wideband as a mean around this problem.

2.1.2 Spectral irradiance and sensor noise

The Figure 1.3 covered noise and power relation, this chapter presents the exact methods used to define and relate these two aspects. There it was demonstrated that the expected power from the star will be $P_{star} = 140\mu W$ for a bandwidth of 10 nm around the wavelength of 590nm, which will be used to define the total power of the wavefront. The power of the wavefront in the model is defined as given in the HCIPy package[11]; squared real absolute values of the electric wavefront field at each point. The total power is just a sum of all the power values and is represented in Equation 2.3. Therefore the power of the wavefront is defined as the square root of the ratio between new and old total power shown in Equation 2.4. Then the magnitude of the PSF or transformed power distribution is shown in Figure 2.2b, and the color bar represents the radiant flux in W.

$$P_{total} = \iint (\Re\sqrt{E(x,y)^2})^2 dxdy \tag{2.3}$$

$$E_{scaled}(x,y) = E(x,y) * \sqrt{\frac{P_{star}}{P_{total}}} \tag{2.4}$$

The camera noise in the model consists of dark noise, photon noise, read-out noise, and quantum efficiency. The dark noise is defined as e/s therefore to add it, it has to be multiplied by the integration time step $1ms$. To simulate the quantum efficiency, the field is multiplied by 0.9 at each integration step. The accumulated signal has the defined power multiplied by the time step, converting the signal from W to Joules. The photon noise and read-out noise are only applied to the final frame provided to the frame generator. The read-out noise follows normal distribution around zero with magnitude from Table 1.3 and is added to the accumulated signal. The photon noise can be modeled as regular CCD noise which follows Poisson distribution or as EMCCD noise which will not be discussed in detail. The example of diffraction-limited PSF for regular and EMCCD at an exposure time of 0.2, 0.6, and 1 second can be seen in Figure 2.3. The EMCCD noise produces a much better result, but for the results to be comparable with the test, regular Poisson noise with increased star power will be used. The images will then have comparable noise, but similar exposure time.

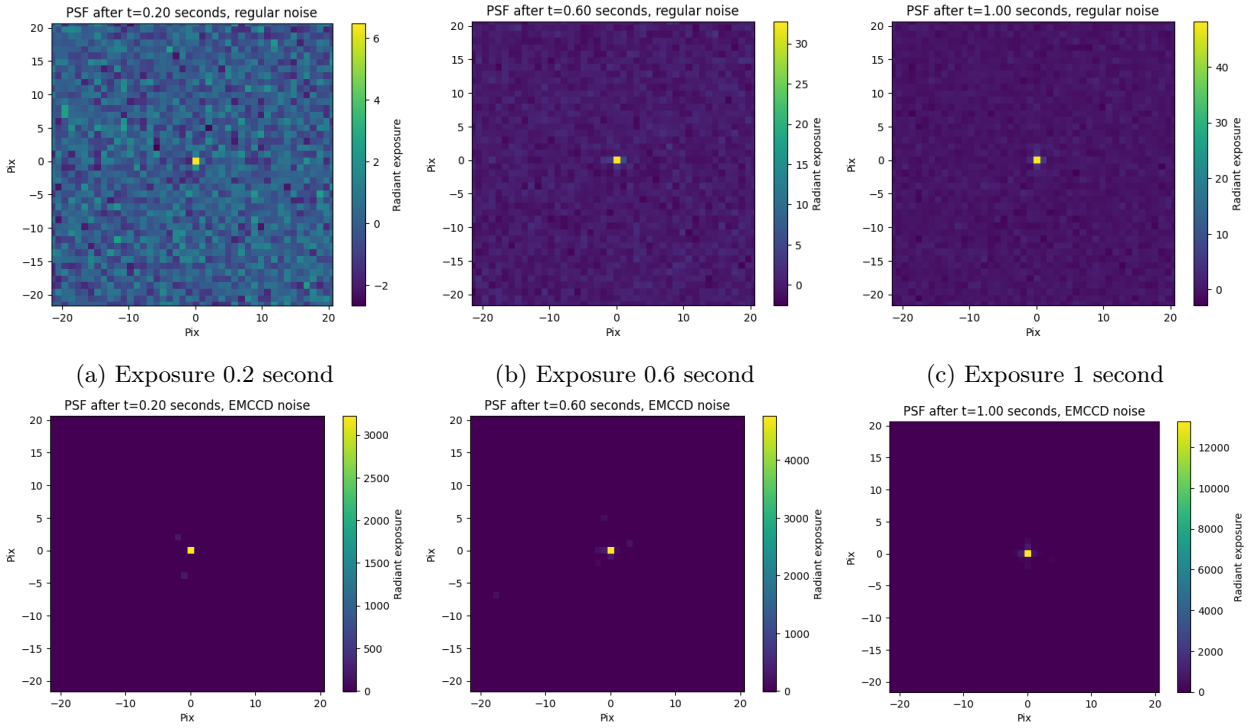

(a) Exposure 0.2 second (b) Exposure 0.6 second (c) Exposure 1 second

(d) Exposure 0.2 second (e) Exposure 0.6 second (f) Exposure 1 second

Figure 2.3: Comparison of different exposure times for regular Poisson noise CCD and EMCCD noise with gain of 200. The top row is regular noise, the bottom row is EMCCD noise. Radiant exposure here is in mili Joules

2.1.3 ASM surface error

The ASM surface error (SFE) will serve as a baseline to be corrected for the algorithm. The SFE of the ASM is defined as a linear combination of 7 modes starting with coma because the first 4 are removed. The coefficients for each mode are chosen randomly from a uniform distribution of values between -1 and 1. Then the cumulative wavefront is scaled to have a PV error of $12\mu m$ from Table 1.2. The example of one of the randomly generated wavefronts with corresponding PSF is presented in Figure 2.4.

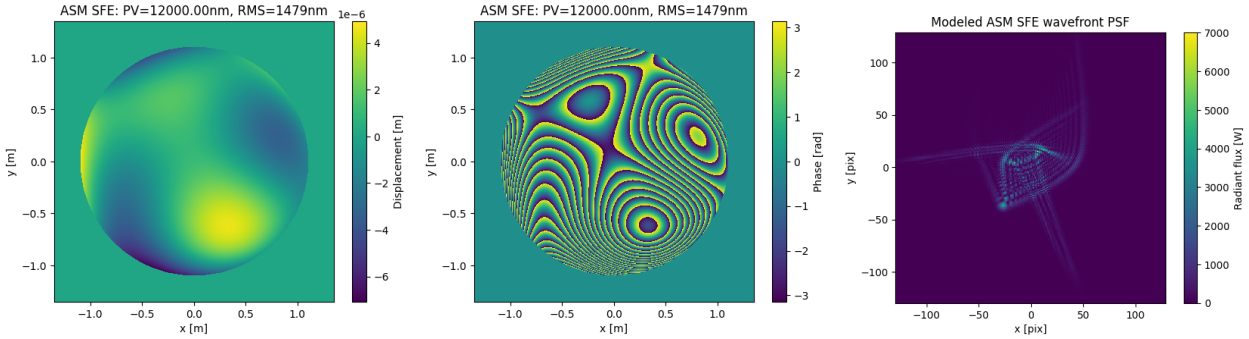

(a) Wavefront simulating ASM SFE (b) Phase of the WF with error (c) PSF of the system with ASM SFE

Figure 2.4: Random mirror SFE according to uniform distribution limited to 12μm PV

2.1.4 Atmospheric aberration model

The atmosphere distorts the wavefronts because of the ever-changing refractive index and thus the light path. The change is typically described with the statistical Kolmogorov model which is a function of layer height, its shearing wind speed, the integrated turbulence strength C_n, and the outer scale of an Eddie L_0. The depiction of a single layer showing different components is presented in Figure 2.5[27]. A flat wavefront is propagated through the atmosphere layer, thus generating an aberrated wavefront. Because the atmosphere is changing rapidly for each frame a new propagation has to be generated. The HCIPy uses the atmosphere layer extrusion method, allowing the generation of a continuous layer[11].

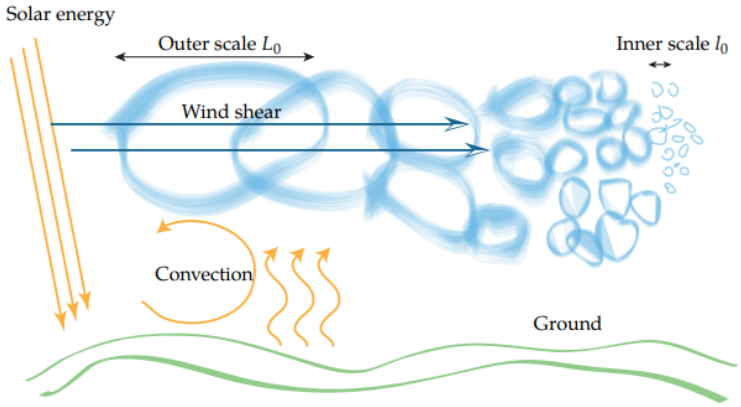

Figure 2.5: A simplified depiction of single layer atmosphere

This method is based on Zernike mode composition, outputting aberration with only the chosen modes. To reduce the modeling time only 10 modes are used to construct atmospheric aberrations. This decision is based on data presented in Figure 2.6[28], it shows a modal decomposition of ground layer aberrations at the Mauna Kea observation site. The piston, and tip/tilt modes are not considered and thus removed. It is clear that with increased order of the mode, the variance greatly decreases. To understand the impact of modeling a different number of modes, data was taken from Figure 2.6 to calculate the increase in variance for the wavelength of 590 nm. The result is presented in the Table 2.1, it is evident that the RMS variance increase from modes to 10 to 15 is only 3%. Even though the increase is roughly 100 nm, when added to 1200 nm SFE RMS, it becomes 1204 nm RMS with a negligible 4 nm RMS increase. Thus it will be considered that 10 modes will be sufficient. The tip and tilt modes will be removed because a separate module with a higher bandwidth is responsible for the correction of these modes.

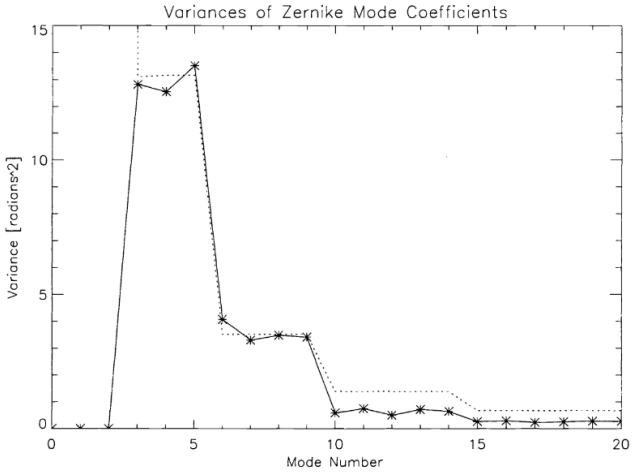

Figure 2.6: Modal decomposition of atmospheric aberration variance at Mauna Kea with Keck observatory[28]

Table 2.1: Cumulative RMS error over the number of modes considered

	5 modes	10 modes	15 modes	20 modes
Cumulative var (rad^2)	39	53.8	56.8	57.9
RMS (nm)	3685	4337	4445	4498
Increase from previous		117.5%	103%	101%

To better simulate a realistic atmosphere, more layers are used. Conveniently the HCIPy package already had a written method for generating a multi-layer atmosphere for the Mauna Kea observatory site, where the UH-88 is located [11]. The examples of various exposures with perfect optics are presented in Figure 2.7. It is evident that the atmospheric distortion results in Gaussian distribution PSF with FWHM of 30 pix. The perfect Gaussian appears only after sufficient exposure, as for short exposure shape and center wander quite a bit. Due to aberrations, the maximum signal is drastically reduced and to artificially simulate EMCCD gain, the signal power was increased by 1e6 W.

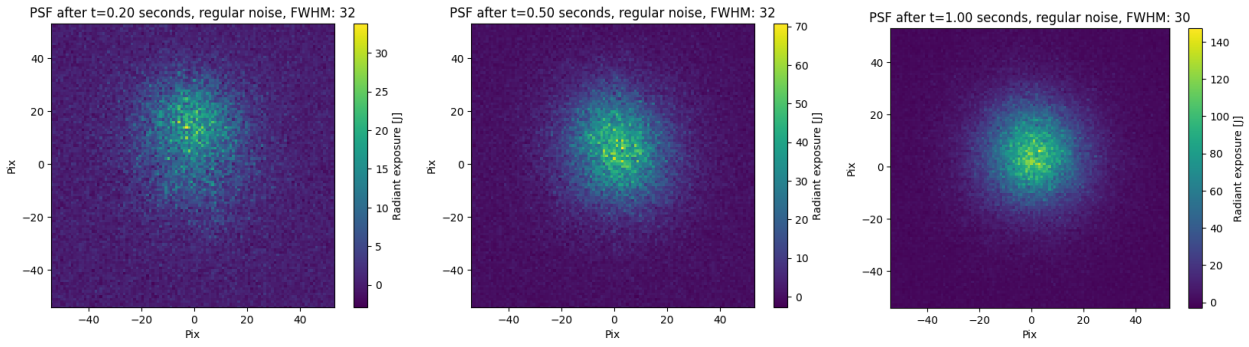

(a) 0.2 seconds exposure (b) 0.5 seconds exposure (c) 1.0 seconds exposure

Figure 2.7: Star light distorted by Mauna Kea atmosphere, observed with perfect optics over different exposure times. FWHM is in pixels.

2.2 Flattening method parts

2.2.1 Image metric: Second moment of intensity

The image quality evaluation is the backbone of this flattening method, as it informs the optimization algorithm whether it is going in the right direction. It will be performed multiple times so it has to be relatively fast. The image will be a matrix where each position holds the intensity value. The simplest metric would be using

the maximum value of the image matrix to direct the optimization toward the optimum mirror shape. Ideally, the optimum would be reached when all the light is concentrated in a single spot thus attaining a much larger maximum when compared to an aberrated wavefront. This method would be fast at evaluating, but because of atmospheric aberrations, the resulting typical Gaussian distribution of PSF the increase in metric will be sluggish. Another aspect is that there are many cases where an increase in maximum might be just a result of an increase in certain aberrations leading to a false positive result - a local minimum. The nature of the PSF distribution in perfect cases naturally leads to slow convergence, and the lack of information within the measure makes it prone to being stuck in local minima. There are quite a handful of different image metrics for various purposes. The image metric named the second moment of intensity (SMI) was appropriate for evaluating a PSF and its distribution around the center, thus having sufficient information for success.

The SMI method is mathematically the same as the second moment of inertia, but instead of mass distribution around the center, the light intensity is used. The evaluation begins with determining the center of the PSF, proceeding with weighing intensity values by how far away from the center they exist. The total value of weighed intensities gives the SMI value, which is further normalized by total intensity. The final calculated value contains the information of the center of the PSF and intensity distribution around that center. Therefore even in the case where intensity increases, but is far from the center, the SMI value will reflect this discrepancy. This makes the cost function smoother which makes it easier for the optimization algorithm to navigate and find a global minimum and not get stuck on local minima. A showcase of the image metric performance on full model PSF is presented in Figure 2.8, here center lines are drawn and the box width takes twice the value of the radius of gyration. The radius of gyration is a term used for the moment of inertia and here is calculated technically the same, but will be called intensity distribution distance (IDD). The exact math is provided in the appendix.

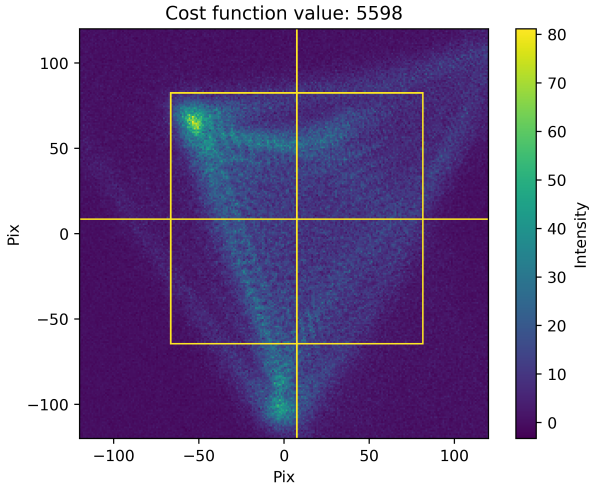

Figure 2.8: PSF with mirror SFE, camera noise, and atmospheric aberrations. The intensity here is measured in Joules, but incorrect magnitude.

Another important aspect is the region of interest (ROI) for the camera, as it determines how much deformed PSF fits into the image matrix. The size of ROI determines the amount of information available for the algorithm, where more information is better. On the other hand, a larger matrix means longer processing times, as well as more noise to filter in case the noise is strong. The image metric determines the distribution length in pixels, thus it is important to keep that distance within the ROI, otherwise, the information becomes useless. In the Figure 2.8 it is clear that not the full PSF is in the ROI, but the PSF intensity radius box perfectly fits. Therefore the determination of ROI size is closely related to the aberrated PSF appearance of the camera, which is related to the optics and the SFE of the mirror.

2.2.2 Cost function performance evaluation

To better understand the possible limitations of the image metric two numerical model tests were carried out. One was designed to estimate the relationship between the wavefront error value and the cost function. The other test was done to find an ideal integration time for the sensor, such that the flattening procedure could

take the least time possible. Both tests yield insight into how to interpret the final result by comparison, which will be discussed in further sections.

Cost variance over different mirror SFE

The cost function and mirror SFE relation for different magnitudes of error will show what to expect from the resulting cost value. The SFE error is modeled as a wavefront, a linear combination of 10 Zernike modes, excluding tip, tilt, and piston modes. Even though the modes are orthogonal, the only possible scaling was done with peak-to-valley and not RMS. This means that there is much more variance in the wavefront, but this is beneficial as the real mirror surface error is unknown. The SFE samples range between $12\mu m$ to $1nm$ with a step of $100nm$, each step contains a batch of 200 independent random WF samples. The samples do not contain either noise or atmospheric aberrations. The Zernike mode coefficients for the wavefront have a uniform distribution which is then scaled accordingly.

The results are presented in Figure 2.9, both axes show an average value of 200 samples, where the x-axis is for image metric and the y-axis is for wavefront error. Both figures show the same average value line, the difference is that each figure shows a different variance of 2σ standard deviation for each sample batch. The left figure in red shows the variance for image metric average values, it is clear that at large SFE the cost value varies significantly, whereas at low SFE the cost almost loses the variance. Meanwhile, the graph on the right in blue shows the variance of WFE RMS average batch value, where the variance remains the same because of the uniform distribution of Zernke mode coefficients.

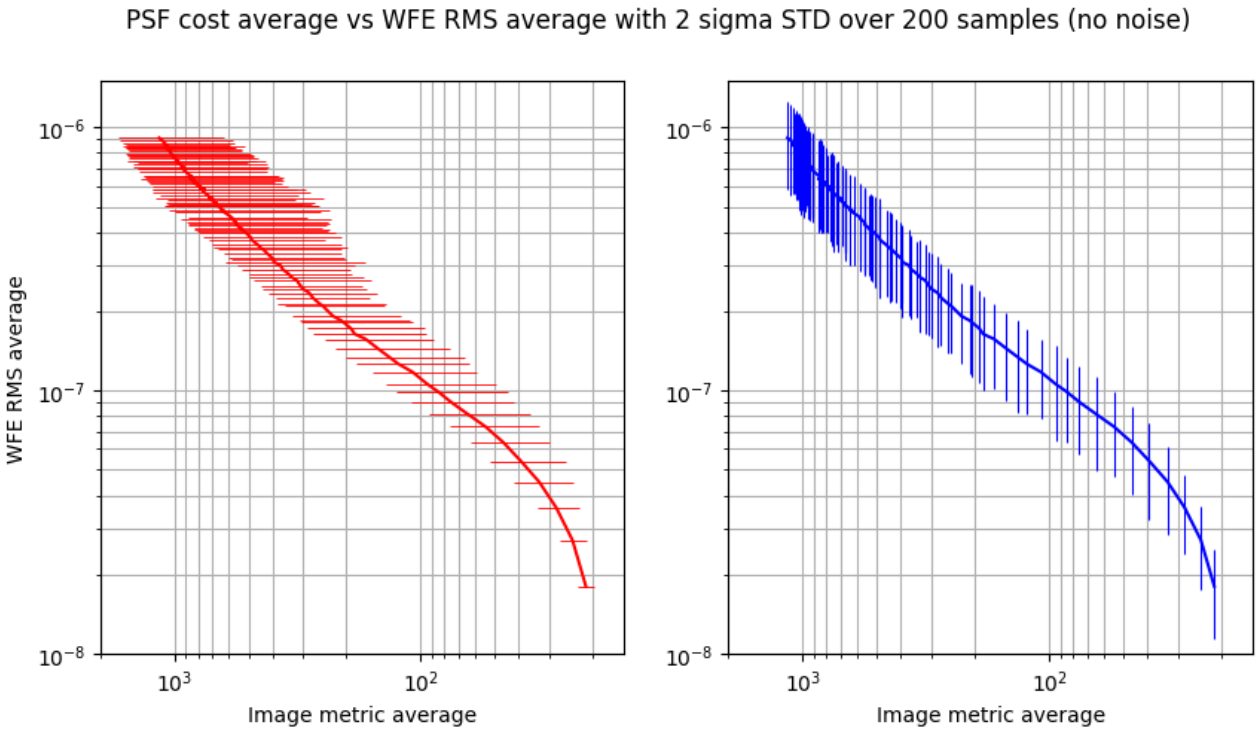

Figure 2.9: Wavefront error RMS average value versus image metric average for 200 random samples at each data point. The left red graph indicates the image metric variance at a specific average. The right blue graph indicates the WFE RMS variance for each average data point.

The Image metric variance drastically decreases with SFE RMS error drop, it is possible to predict the SFE of the mirror with greater accuracy. This also might mean that metric performance might be lower because the distribution of PSF is very close to the center. Different modes induce different shapes of PSF, when the error of a particular mode is large it is easy to determine whether it has been improved. When the SFE is low, the mode-specific PSF shape overlaps with other modes-produced shapes thus the change in the coefficient of the mode does not produce a noticeable change. This means attaining an excellent SFE will take longer than reaching a mediocre result.

Allan variance for image integration time

The second numerical model test is based on the statistical analysis termed Allan variance used for oscillators and gyroscopes. The image metric analysis is used to determine the best image integration time where the cost function will be most accurate with atmospheric aberration and camera noise present. The variance of the cost function is evaluated over increasing windows of exposure in a large data set. To compose this large time series data set for each time step of $1ms$, a flat wavefront is passed through a changing atmosphere, added together with a static wavefront of mirror SFE which is then Fourier transformed to produce a single time step PSF. To determine the variance for an integration window length, multiple windows of that particular length have to be evaluated. The more windows evaluated the more accurate variance of the cost function. To achieve a large number of windows within a limited time step data set, the windows are overlapping thus increasing the variance accuracy. This also lets us evaluate larger windows of the same length as the data set. Because the construction of such images is a very time-consuming process, the number of windows is not static and decreases with the integration time window. This means that the confidence in variance decreases with the integration window length. Naturally, to get the value at a longer image integration time, the scanning windows are made larger with each iteration. The exact math used for the method can be found in the appendix.

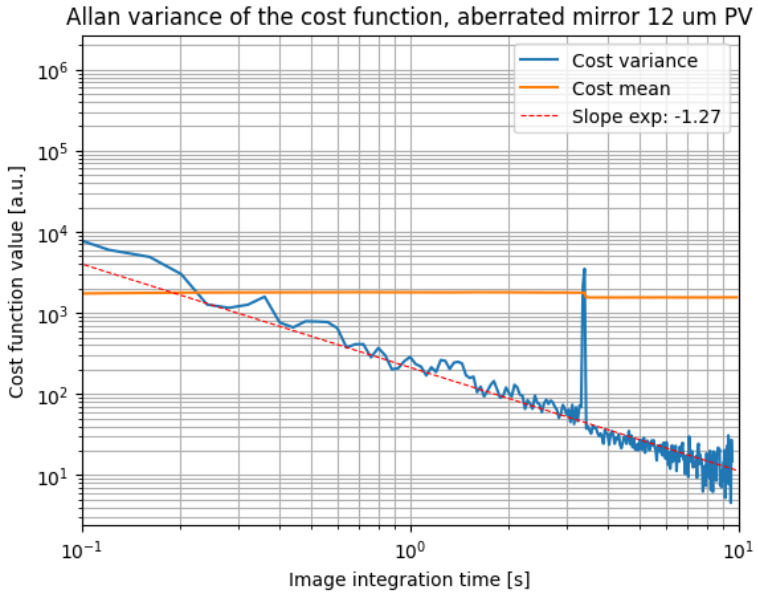

Figure 2.10: Allan variance of cost function value over the image integration time with $12\mu m$ mirror SFE

The result for SFE of $12\mu m$, typical Mauna Kea atmosphere, and EMCCD levels of noise is presented in Figure 2.10. The blue line shows the relation between cost function variance and image integration time. As expected the variance decreases with an increase in exposure time, the data becomes more noisy as fewer windows are used to calculate the variance. There is no clear floor for the decrease in variance with an increase in exposure time, thus it is not unreasonable to choose exposure length where the variance is the same as the mean cost value at $0.2s$. The orange line represents the mean cost value of the PSF over multiple samples of the same window size indicating that the SFE of the mirror stays the same. The red dashed line represented the trend in the drop in the variance with the exponent slope of -1.24. The strange outlier seen as a jump is most likely due to a bad cut in the large data set, due to computer memory limitations.

The test was carried out for the case where the mirror was perfectly flat to examine whether the would be a limit with an ideal wavefront. The decrease in variance is almost the same as in a completely deformed mirror with a trend-line slope exponential of -1.24. Although no floor for the cost function was observed, the variance in cost mean value was less consistent than with large SFE. A similar conclusion can be drawn as with the first test that the image metric capabilities at low SFE greatly diminish. A similar slight jump in variance occurs at the same place as the outlier in the large SFE variance, the reason is unclear.

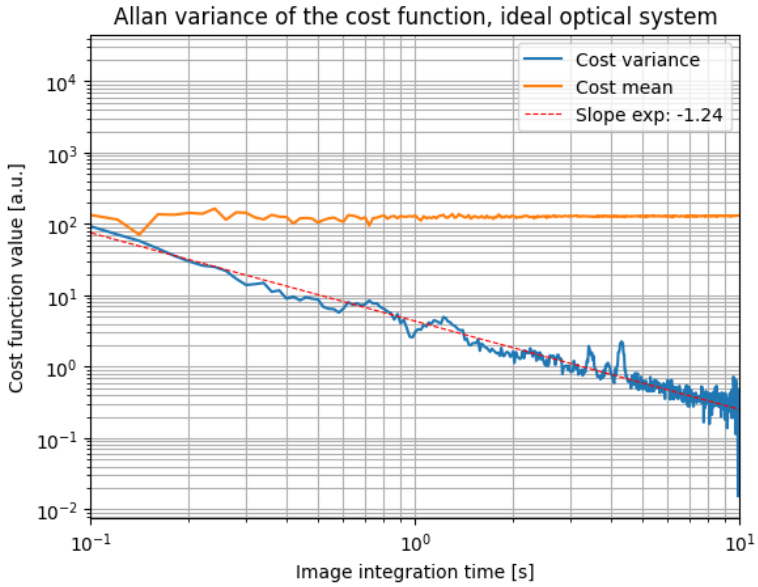

Figure 2.11: Allan variance of cost function value over the image integration time without mirror SFE

2.2.3 Optimization algorithm

Where the image metric is a horse of the control method, the optimization algorithm will be the carriage. There are many different algorithms to be used with high efficiency, especially the ones using second-order derivatives of the cost function. From the image metric analysis, it can be seen that the cost function would be non-smooth and this property does not allow obtaining those derivatives. Thus to set the method for success a more robust and simpler direct search algorithm is chosen, preferably one that is more suitable for optimization of a moderate amount of variables. This type of algorithm treats the problem as a black box where it can access and control some variables and get an output that directs its search direction.

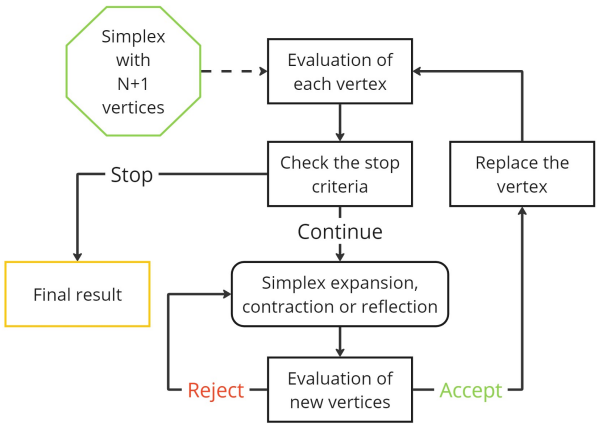

Figure 2.12: Nelder-Mead simplex optimization algorithm working scheme

One of the more robust optimization methods is Nelder-Mead, which uses an $N+1$ sample point to create a simplex. Its generalized optimization sequence is presented in Figure 2.12. The simplex shape in two dimensions will be a triangle, and in three dimensions will be a tetrahedron. Each vertex has coordinates for the black-box input which evaluates the cost function and assigns that value to the vertex. Then each vertex is compared and the simplex can flip, expand, or contract thus scanning the search space of the cost function, these optimization cycle continue until termination conditions are satisfied. The several termination conditions are either some number of total cost function evaluations or a tolerance value for cost function improvement. If the cost function for each vertex of the simplex does not change the cost function more than the tolerance value the optimization is terminated. The function evaluation is a hard limit stop, whereas the tolerance stop is a sufficiency stop.

The rather simple optimization sequence of the two-dimensional cost function is visualized in Figure 2.13. The simplex is chosen manually at x_1 and x_2 with vertices being at $[0, 0], [0, 1], [1, 0]$. For each point, the cost function is evaluated and evidently, the $[0, 1]$ value is the worst out of all three. Thus this vertex is flipped over $[1, -1]$ point, the flipping axis being two other points. Then because further flipping would not improve the cost function value, the simplex is shrunk from the worst point. This allows us to refine the search and find a better solution. The simplex can also extend as can be seen in the 7th step. In higher dimensions, the simplex will become naturally larger, and for 10 Zernike modes becomes a matrix of size $N \times N + 1$. The coefficient values are constructed by multiplying the identity matrix with the chosen value and then adding a row of zeros.

The plot's contour values indicate a minimum at coordinate $[2, 1]$, and all the values decrease towards that minimum. This means that its Hessian is positive definite, thus having a clear minimum within that area. This is an ideal case where there is a single global minimum. Given the nature of the previously discussed image metric, a similar property can be expected. This is because the PSF distribution around the center will increase regardless of the Zernike mode coefficient sign. Therefore convergence of the algorithm should be guaranteed.

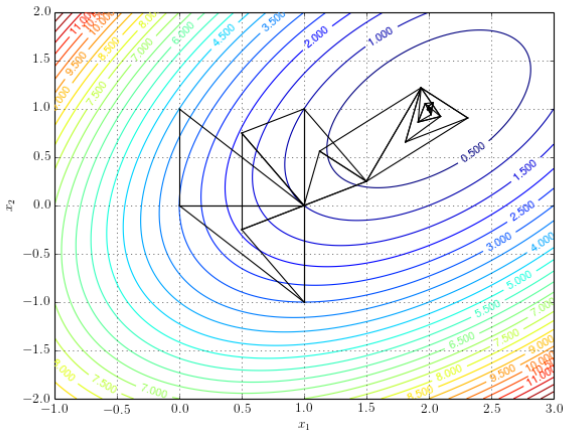

Figure 2.13: Nelder-Mead optimization procedure in simple 2-dimensional case

The simplex vertex coordinates are usually chosen manually based on the knowledge about the system that is to be optimized. A natural guess would be zero, because in the system that is controlling the coefficient of the Zernike modes, where zero would have the least aberrations. However, this is not the case where a simplex is used to search the cost function space. From Figure 2.13 can be seen that if all the coordinates of the simplex are chosen zero, this would make it infinitely small. Potentially it could become larger by expanding, but it will take numerous function evaluations to determine that it needs to expand, thus taking much longer to converge. In the case where simplex positions would twice twice as large, each flip of the simplex would result in a similarly poor cost function value. This then would require additional shrinking of the simplex and again would take additional evaluations. In the example case, to have the least evaluations would be best to start as close to cost function zero, which is at $[2, 1]$. It is clear that choosing a simplex vertex position is a sensitive matter requiring expected values of the search field. It can be concluded that the simplex size has to be on a similar scale or larger than the cost function gradient values. This then ensures that the simplex will be able to search the space without performing unnecessary function evaluation to expand or contract to find the correct size. For the modeled system the maximum expected SFE is $12\mu m$, and the initial simplex was chosen to be 10 times smaller at $1.2\mu m$.

2.3 System model parameters and performance

To answer the main question of whether the method can shape the mirror to the desired quality the full system has to come together into a single system. The representation of this system is depicted in Figure 2.14, where the physical model contains a star, atmosphere, DM, and camera. The star is modeled as a flat wavefront with UH-88 pupil diameter and an estimated power level of Sirius A. The atmospheric aberrations distort that ideal wavefront which is then combined with the deformed mirror wavefront to be transformed into a focal plane image. The camera-specific noise is added to the image for each time step of $1ms$ depending on the integration time. The image is then passed to the image metric to evaluate its quality as a cost function value

for the optimization algorithm. The optimization algorithm navigates the search space by controlling the mirror wavefront through the coefficient of the Zernike modes and attempting to improve the cost function value.

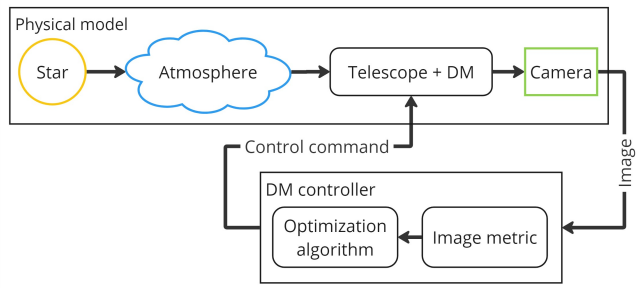

Figure 2.14: Representation of modeled parts of the system

Ten trials were carried out to determine if the flattening goal for WFE of $100nm$ RMS is reached within the time limit of 10 min. Each trial started with a random mirror WFE, but with a determined seed such that experiments are repeatable when parameters change. The nature of the Nelder-Mead optimization algorithm is evaluating the function at multiple positions determining the worst, and then flipping the simplex making some evaluations potentially even worse. Thus the convergence of the cost function becomes non-smooth. Even if the recorded values would only contain the improved cost function, the non-smoothness would persist due to the camera noise present in every observation. Several parameters are tunable to adjust the process and its outcome, namely the number of cost function evaluations, the cost function comparison tolerance, camera ROI, and the initial starting position for the optimization.

2.3.1 Termination tolerance and function evaluation limit

The termination tolerance determines the final result compared to the initial value and is set to be 0.005 % which was found by trial and error for this specific problem. Lower tolerance results in being ineffective and the optimization is then terminated by the function evaluation counter. Larger tolerance would mean a premature stop, resulting in poor results. The evaluation count determines the total optimization time depending on the length of a single evaluation. These two parameters do not influence the result directly but determine which is the last result. Letting the algorithm run by setting either more evaluations or low termination tolerance does not improve the result further compared to a hundred evaluations. This can be observed in Figure 2.15, where the only difference between the tests was the termination tolerance. The optimization converges at roughly 150 function evaluations for these particular optimization settings and does not improve the result further. This is because the the floor of best result is determined by the image metric as the cost value gradient decreases with smaller WFE, this was also observed in Figure 2.9 with a decreased variance of the metric value.

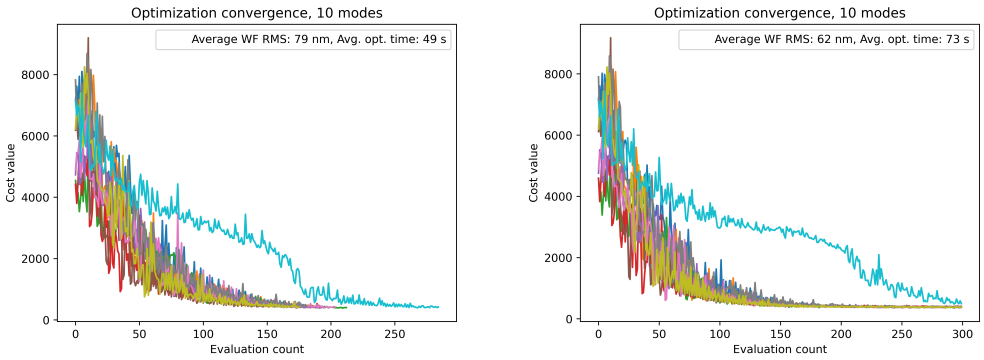

(a) Termination tolerance at 0.005 %

(b) Termination tolerance at 0.001 %

Figure 2.15: Convergence of optimization algorithm for different termination tolerances with 0.2 seconds exposure, controlling 10 modes. The camera ROI is 340x340 pixels for the image metric. The simplex at $0.5\mu m$

2.3.2 Camera region of interest and initial optimization guess

The parameters affecting the performance of the method are initial guess simplex coordinates and the ROI of the camera. To illustrate the effect of simplex size the optimization test with similar settings was carried out and their cost function convergence is presented in Figure 2.16. Both tests are with identical settings of 0.2 seconds exposure, controlling 10 modes and the same initial mirror SFE for each trial. The only difference is the simplex size where the left figure has it at $1\mu m$ and the right at twice the magnitude lower than expected mirror SFE, $0.1\mu m$. Comparing the performance of each, it is evident that the smaller simplex has a much smoother cost history because of the small initial simplex step. It cannot enlarge itself to search for a global optimum as the non-smoothness never increases to the magnitude of the left graph. For some trials, this results in the algorithm getting stuck on local minima without reaching a satisfactory mirror shape. On the other hand, simplex being only a magnitude lower than the expected error has very good convergence with low final SFE. Although the recorded history of the cost function is extremely non-smooth, it indicates the algorithm's property to jump over local minima if the simplex is chosen correctly. In the case of a larger simplex, the non-smoothness becomes too large, and takes many more evaluations to decrease the simplex size to be able to converge. In the case of flattening the mirror, it is reasonable to choose the simplex to be a single order of magnitude lower than the expected mirror SFE.

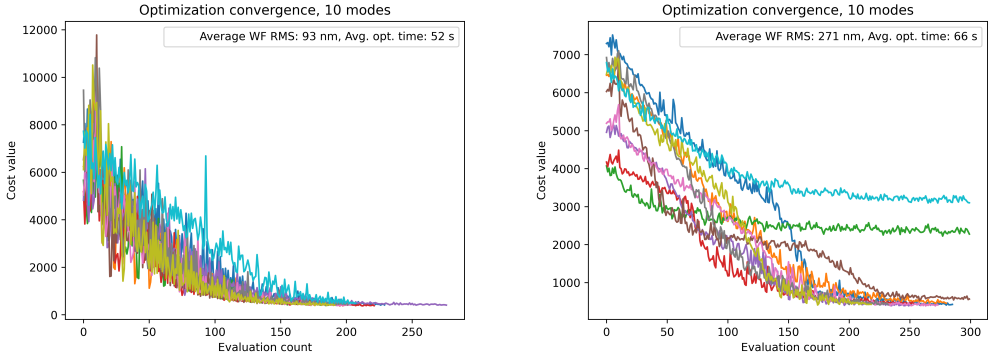

(a) Simplex at $1\mu m$

(b) Simplex at $0.1\mu m$

Figure 2.16: Convergence of optimization algorithm for different simplex magnitudes with 0.2 seconds exposure, controlling 10 modes. The camera ROI is 340x340 pixels for the image metric. Cost function tolerance of $5e-3\%$

The other important parameter to control is the image region of interest, which determines the quantity of information available for the image metric. It also influences the number of pure noise pixels against the pixels receiving light. Comparison between initial and final frames optimization frames with ROI sizes of 340, 240, and 140 are presented Figure 2.17, all the other parameters are the same. The increase in size from 240 to 340 does not show any significant change, whereas the difference between 240 and 140 ROI is noticeable. The IDD box becomes larger relative to the PSF with increased ROI, this is due to the pixel with noise and more PSF being observed. Where the ROI is 140, a significant portion of the PSF is outside of the range resulting in unobservable changes of the PSF during the optimization. It naturally leads to poor performance, evident from the final result with WFE 407 nm RMS with similar or worse performance in additional trials. Clearly, it shows that the size of ROI is required to be at least twice the size of the IDD box width for the method to converge to a decent result.

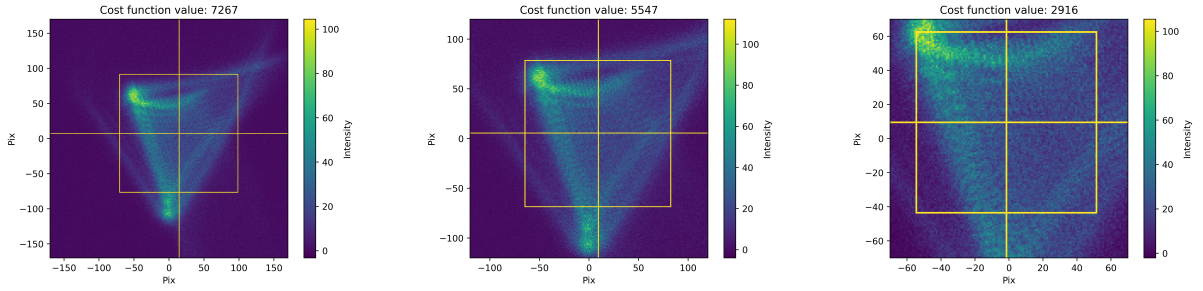

(a) ROI of 340 pixels in width (b) ROI of 240 pixels in width (c) ROI of 140 pixels in width

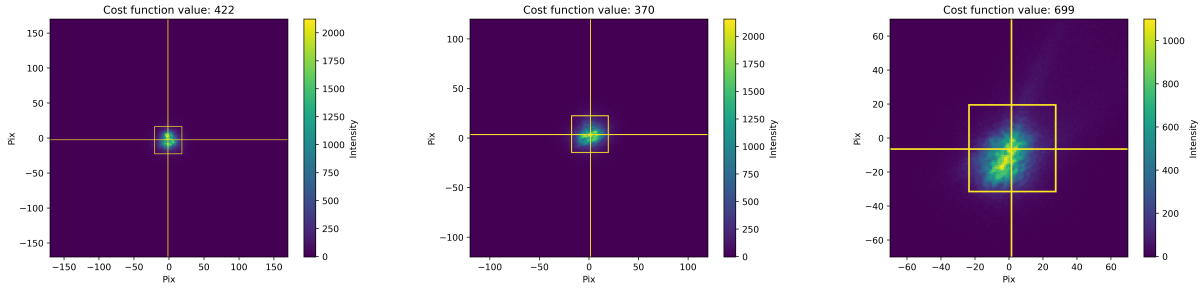

(d) PSF with WFE of 115nm RMS (e) PSF with WFE of 144nm RMS (f) PSF with WFE of 407nm RMS

Figure 2.17: Optimization of trial 1 with different sizes of ROI of the PSF image. The top row shows the initial images whereas the bottom the final optimized PSF results respectively

2.3.3 Optimization results

With tuned optimization parameters the algorithm is able to bring the mirror SFE from 12μm PV to the desired remaining WFE result of 100 nm RMS. The method uses 10 modes to control the mirror and correct the SFE wavefront constructed from the same 10 modes. The result is achieved over multiple trials with different initial mirror SFE within the time limit of 10 minutes. The simplex is an identity matrix with values of 1μm and camera image ROI of 340×340 pixels. The maximum number of evaluations was set to 300 and the termination tolerance at 0.005, of the trials were terminated by the cost function tolerance. The convergence of the test is presented in Figure 2.18 where all trials are consistently converging with an average result of 93nm within 52 seconds.

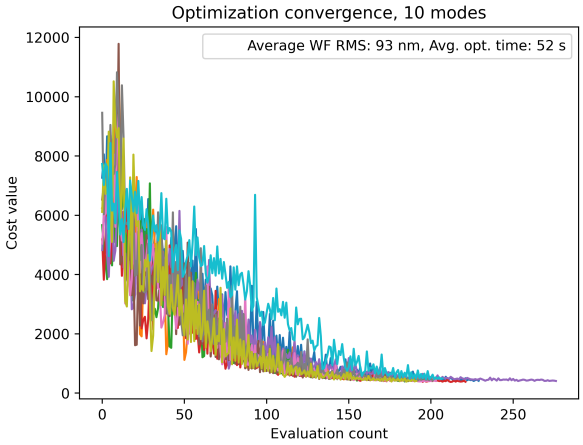

Figure 2.18: The cost function convergence of flattening method consisting 10 different trials.

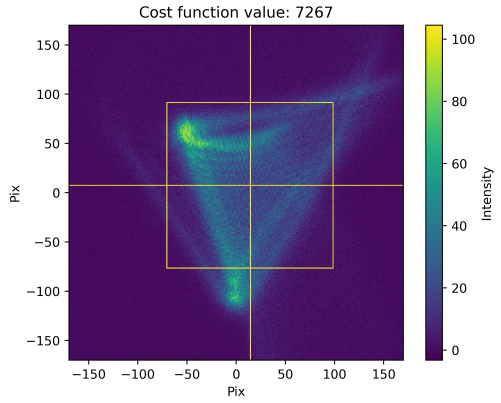

(a) Trial 1 initial frame

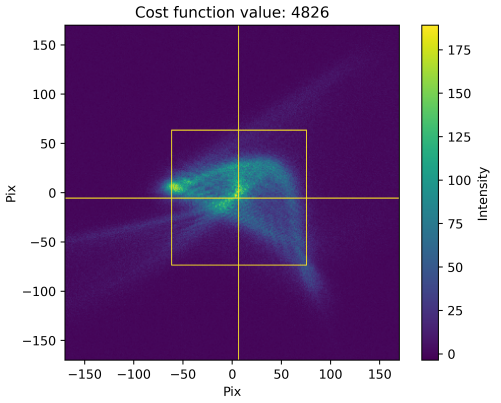

(b) Trial 5 initial frame

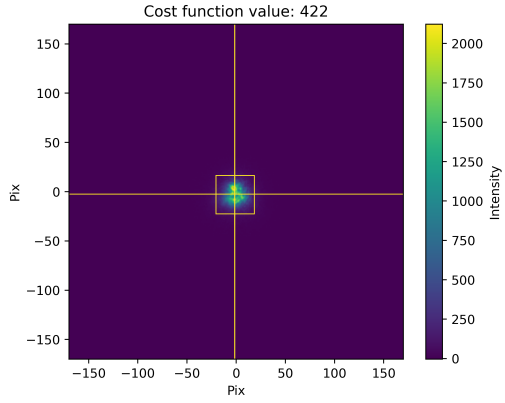

(c) Trial 1 final frame, remaining WFE 51 nm RMS

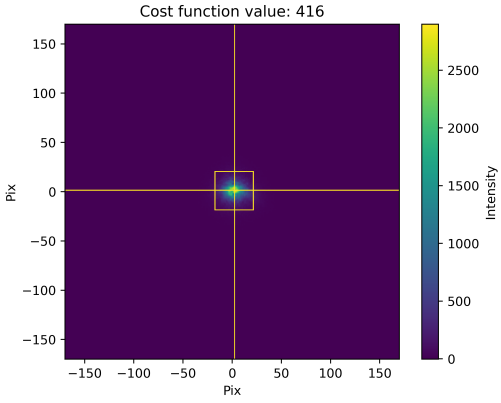

(d) Trial 5 final frame, remaining WFE 119 nm RMS

Figure 2.19: Trial 1 and 5 initial and final frames from the optimization process. The exposure time for all trials is $1ms$.

The first and fifth trials with their initial PSF and final result are presented Figure 2.19. Although the initial PSF is much larger and has a cost value of 1.5 times of the 5th trial, the final result is twice as good when comparing the WFE. Another important note is that even though the cost value of the final result seems very close, the 5th trial appears to have a smaller PSF and has lower image metric value with twice the remaining WFE. This supports the notion that the image metric at low WFE is not sensitive enough to reflect that error difference in the cost value.

It can be concluded that the numerical model is able to achieve the goal of shaping the mirror to perform as a passive mirror within the given time limit. The model contains the most influential parts and their characteristics of the physical UH-88 system. However, there will be discrepancies between the model and the UH-88 which will change the performance of the method. This might be attributed to Zernike modes not fitting the actuator pattern leaving an unactuated surface error, as well as differences in camera noise or its performance. To analyze and understand the capabilities of the shaping method a physical optical setup with DM was built to conduct a performance test.

Chapter 3

Flattening method testing

This section presents the experimental validation of the flattening method using a physical deformable mirror (DM) setup. The objective is to assess the method's applicability in a real-world environment and identify any unmodeled factors that may influence its performance. By replicating key components of the UH-88 telescope system—including the light source, DM, and camera—the experiment aims to simulate the conditions under which the flattening method would operate. Detailed descriptions of the optical layout, component specifications, and assembly processes are provided. The testing involves optimizing the image metric both with and without simulated atmospheric aberrations, utilizing Zernike modes for mirror control and the Nelder-Mead optimization algorithm. The results confirm that the flattening method effectively reduces the mirror's surface errors to the desired levels, aligning with the numerical model's predictions and offering insights for future implementations.

3.1 Optical layout and specifications

To simulate the UH-88 system three most important components are the light source, deformable mirror, and camera to observe the PSF. The light source is designed to simulate a star as a point source, the DM has identical actuator architecture except for the layout, and the camera pixel size is matched to have the same ratio as UH-88. To bring these parts together other optical components are required, the representation of these parts with the setup is shown in Figure 3.1. The diverging light from the source is reflected with a beam splitting (BS) mirror to the telescope with an achromatic lens which collimates the light onto the DM. The reflected light from the mirror passes back through the BS into the camera. The optical setup conveys the basic idea of how the telescope would work and enables the test of the flattening method.

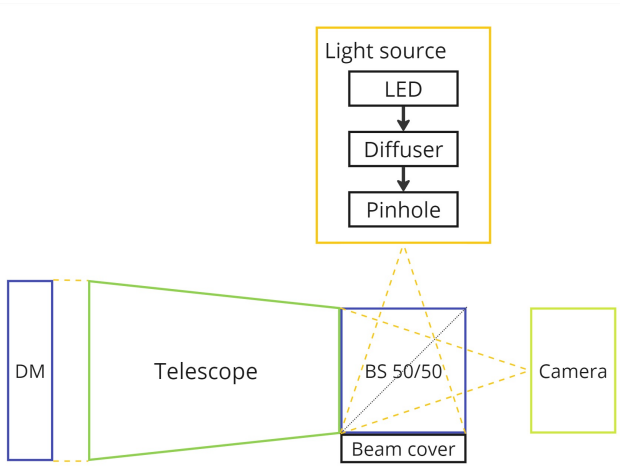

Figure 3.1: Representation of optical system and its components

The light source, camera, and beam splitter (SCB) units are assembled using the Thorlabs cage system to keep optical components centered on the optical axis. This assembly is coupled to the telescope through several threaded adapters bringing all the components to the same optical axis. The whole unit was mounted on the Z stage to control its height relative to the table with micrometer precision. During the measurements it was seen

that the SCB was vibrating from slight adjustments as it was far from the fixation point under the telescope. To increase the stiffness of the assembly additional support under SCB was added significantly reducing the jitter of the PSF on the sensor. Utmost care was taken to not over-constrain the whole assembly, but in this case, it was unavoidable and the worst induced aberration would be either tip or tilt. The DM is fixed to the kinematic base which was used to control the tip and raise it to the correct height.

The beam path between the optical components was covered by black paper to isolate the system from the room lights and convection inducing additional aberrations. The radiator of the LED and the camera body were left outside of the isolation box due to being sources of heat that would cause convection within the box. The covered full setup is presented in the Figure 3.2.

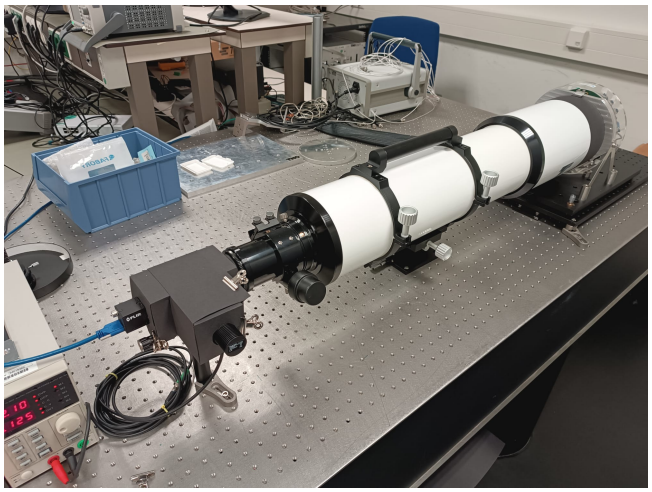

Figure 3.2: Assembled optical system with light path isolated from convection, environment illumination, and heat sources.

3.1.1 Light source and routing assembly

To simulate a star as a point source a narrowband light source is assembled from M590L4 LED, engineered diffuser, and pinhole. The M590L4 LED has a wavelength centered at 590 nm with a bandwidth of 10 nm. The ED1-S20 engineer diffuser has a transmissivity of 90 %[29] and uniform light intensity distribution over a 20-degree angle. The P5K pinhole diameter of $5\mu m$ was chosen to match the diffraction size of the UH-88. It is mounted in a stage that can translate in X and Y directions perpendicular to the optical axis which allows adjusting its image position on the camera. Because the BS reflective surface is not the same distance from the entry and exit holes, its optical axis shifts by roughly $0.7\mu m$, which requires positioning of the light to bring it into the center of the camera.

The rough irradiation falling onto the camera can be calculated from the specification sheets of the optical and LED components. The maximum irradiance at 200 mm is $6\mu W/mm^2$, but since the diffuser is much closer to the LED the intensity over the area will increase. The light from the LED leaves at half of a circle in roughly uniform intention, which is not far from the specifications. With this estimation, the change in density can be described by the function for the area of the half circle presented in the Equation 3.1. The distance between the diffuser and LED is 4.5 mm, which results in a circle area being 1976 times smaller than at the distance of 200 mm. This meant that the light density was almost 2000 times larger at the diffuser, resulting in $11mW/mm^2$.

$$A = 2 \cdot \pi \cdot r^2 \tag{3.1}$$

The diffuser has a specially engineered surface the light leaving it has a non-Gaussian uniform distribution, thus the concentration of the light at the pinhole will be higher than with a regular diffuser. The distribution of intensity for a 20-degree angle is presented in Figure 3.3. The field of view half angle for the lens is 4.84 degrees, and the pinhole will be at the focus thus an exact cone of light from the diffuser will fall through the pinhole and through the optics. With the distance 30 mm between the diffuser and the pinhole this results in $20.3mm^2$ area on the diffuser from which the light will be seen. The radiosity is multiplied by the 90% transmittance of the diffuser and the area, resulting in a radiant flux of $201mW$.

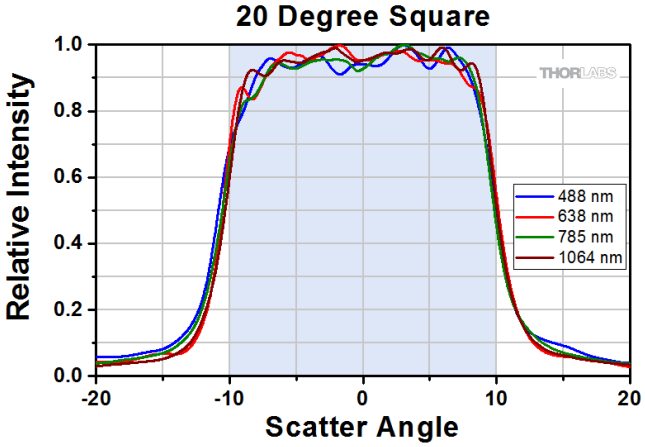

Figure 3.3: The intensity distribution for the engineered diffuser

The CCM1-BS013/M beam splitter with 50:50 reflection coating for the wavelength range of 400-700 nm, with the transmission of 47% for light at 590 nm. Because it is 50:50 BS, the light after the first reflection is half of the initial light, then when it passes back a second reflection occurs and half of the light goes towards the LED and the other half goes to the camera. Therefore, in the end, only a quarter of the original light intensity ends up at the CMOS sensor, accounting for transmittance the exact coefficient will be 0.249. Assuming a collective 97 % transmittance of the achromatic telescope lens and the mirror the final radiant flux reaching the camera will be $50mW$. Accounting for the 65% QE at a particular wavelength of the sensor only $32.5mW$ will be observed. Accounting for the QE ratio of EMCDD and the test sensor being 1.4 the irradiance will be 167 times larger than the estimated irradiance of $0.14mW$ from Sirius A in the requirements chapter. To compensate for the extreme noise of the camera it was required to keep the intensity at such a high level. The exposure was set to $9ms$ as it seemed to have a good signal-to-noise ratio.

3.1.2 Camera and noise filtering

The camera used for the test is a CMOS which is significantly more noisy than the regular CCD sensor, and much more than an EMCCD. A simple high-pass filtering technique was used to clean up the noise. To achieve this a sample with the size of 50 by 50 pixels is taken from the corner of the image matrix. The lowest value and average of the sample are determined, where the lowest value is subtracted from the whole image. The image pixel values that are below 3.5 times the average sample noise are set to zero. Although this does add additional computation time it will not be necessary in UH-88 thus the filtering time will be subtracted from the evaluation. The filtering greatly improves the performance of the image metric. Additionally, to ensure that the full pixel depth range is used, an automatic gain adjustment was enabled. If the measure maximum value of any pixel would hit the full well depth of 16 bits, the gain would be lower. This way higher intensity value range is prioritized while the filtering will cut off the lower values.

3.1.3 System optics analysis

To help interpret the final result and understand possible sources of WFE due to the optics of the system, it is necessary to analyze the optical system. Without a WFS it's not possible to measure the wavefront directly, thus an alternative method is required. The Roddier test is exactly that, which uses one image before the focus and another after the focus. The difference in intensity is then used to recreate the phase of the wavefront and is similar to the curvature WFS principle. The same optical setup was used, but instead of DM a flat mirror with $\lambda/16$ RMS surface error was used. It is expected that the telescope lens to be the major source of error, thus documentation will be used to analyze the system.

The telescope 20-TS-Optics contains an achromatic lens with a diameter of 152 mm and a focal ratio of 5.9 is used to collimate the point source diverging the light cone onto the mirror. It is a refracting telescope which means that its pupil does not have any obstructions and will be similar to the model. The best optical performance with the least aberration of the specific achromatic lens is shown to be at a wavelength of 590 nm and is presented in Figure 3.4. To have the least aberrations induced by the system the LED wavelength was chosen to be at 590 nm. Notably, the aberration over the full aperture has the profile of primary spherical aberration which is the 11th Zernike mode. Although its scale is too large to accurately determine the exact error.

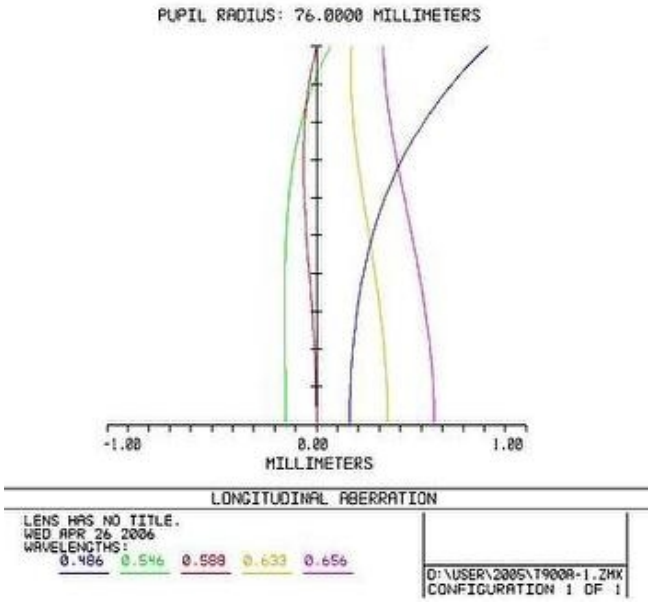

Figure 3.4: Telescope achromatic lens longitudinal aberrations for different wavelengths.

The WFE measurement with intra- and extra-focal images was invented by the well-known french astronomer François Roddier and developed into software by other astronomers. The method was favored by amateur astronomers as the only required measurement device was a camera and some precise stage to move the camera back and forth. The main working principle of the measurements is presented in Figure 3.5, where two images before and after focus at the same distance are required. The two images are subtracted from each other to produce the signal which results in a difference in the intensity which is used by the algorithm to iteratively recreate the wavefront. In the software documentation, it is mentioned that the algorithm uses using Fourier transform and is iterative, which might be very similar to the Gerchber-Saxton phase recreation algorithm.

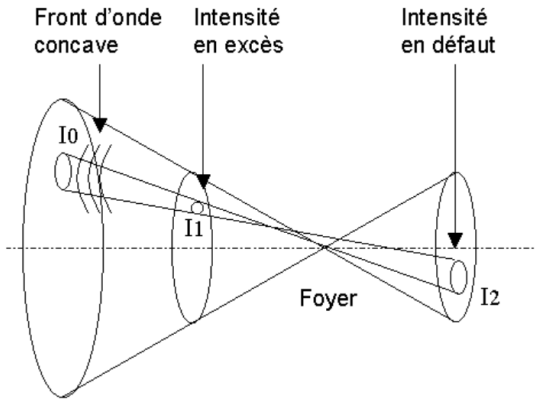

Figure 3.5: The principle of Roddier test

For the test, there were 3 distances used 3, 4, and 5 mm. Each distance had 5 images taken at the intra-focal position and 5 for extra-focal. This was done to average out any possible error zero mean error within the system or the measurement method. The results are presented in Figure 3.6, where each distance 5 experiments are plotted as average starting from 5th mode, astigmatism. The 4th mode defocus is removed as it can be easily controlled with the linear stage of the camera. The 2nd and 3rd tip/tilt modes are controlled with the DM and thus removed as well. The consistently largest modes are 5, 6, 7, 8, 11, 16, and 17, where 5th and 6th are primary astigmatism, 7th and 8th are primary coma, 16th and 17th are secondary coma, and finally the 11th are a primary spherical aberration. All of these except the 11th mode are off-axis modes, meaning that they are induced whenever the light source is displaced perpendicular to the optical axis. Indeed the point source was displaced from the axis because secondary reflections were overlaying with the extra and intra-focal images.

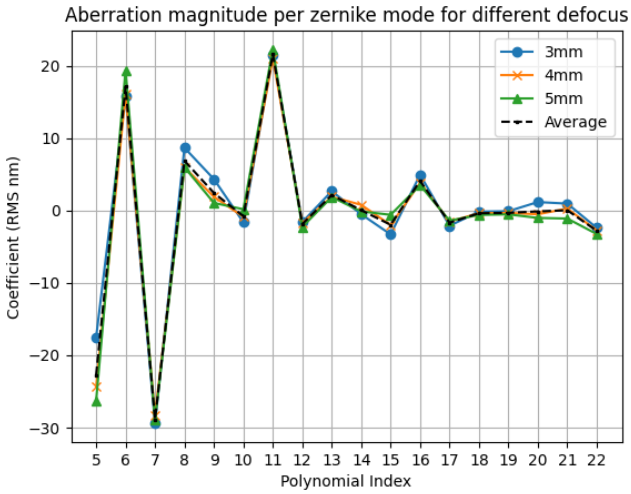

Figure 3.6: Roddier test data from 3 different focus distance and their average.

The 11th has the same profile as indicated in Figure 3.4 confirming the data sheet with the resulting error of 20 nm RMS. The algorithm documentation mentioned that the error of the algorithm is within 100nm RMS error, although the result seemed relatively consistent without such error. The wavefront with the modes combined had the error of 250 nm PV and 48 nm RMS. Some of the aberrations might be amplified by the beam splitter as per documentation its transmitted wavefront error is specified to be 147 nm RMS, which clearly does not seem to reflect in the results. The resulting SFE is small enough to be indistinguishable using the image metric and will merge with the surface error of the DM. Thus it should be possible to reach the desired result of 100 nm RMS for mirror SFE.

3.1.4 Mirror mode control

To control the mirror a combination of Zernike modes was used. To position the actuators the wavefront was sampled at respective positions and then converted to the control current. To make the conversion the maximum current of 0.15 A and maximum inter-actuator displacement of 20μm ratio was calculated. This ratio is used to convert the wavefront displacement to the current. An example of the wavefront and the actuator position with their displacement is presented in Figure 3.7. Notably, the actuators have rectangular placement which differs from the ideal hexagonal placement for UH-88 ASM. Due to this arrangement, there will be inaccuracies between control and actuated modes, as was presented in Figure 1.1.

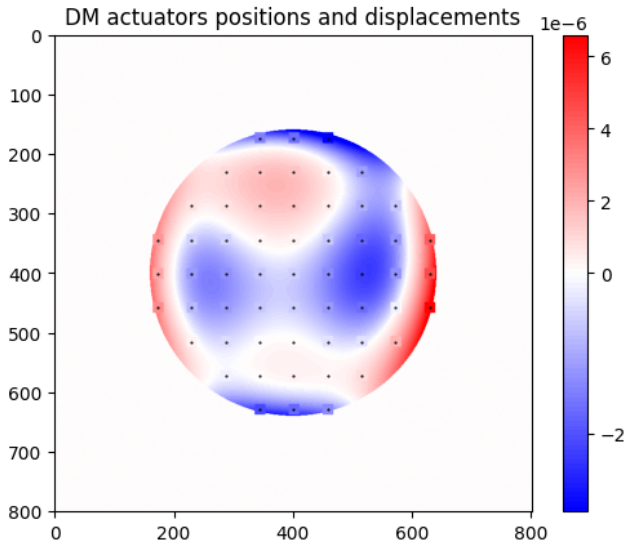

Figure 3.7: A combination of 10 Zernike modes with random coefficients with actuator positions as black dots

3.2 Optimization of image metric

The DM initial error according to the previous test was 15.5μm and 2780nm RMS which is similar to the expected values for the UH-88 ASM. To verify the flattening method tested in the model and analyze its capabilities first the test without imitation of atmospheric aberration is done. The optimization settings are almost identical with few changes to the simplex size, exposure time, and additional noise filtering for the images. Due to high noise, and multiple modes, the cost function was extremely non-smooth, and the termination tolerance was unable to stop the algorithm at the convergence. Therefore the function evaluation count was used to terminate the algorithm. To acquire as much information as possible each shaping trial was allowed to run for a limit of 10 minutes. After extensive testing of different parameter influences for the process it was found control of 118 modes achieved the best convergence. The possible reason for this might be that some modes fit the actuator arrangement better and can compensate for the modes that do not fit well. After decent results were achieved in the plain test, the simulated atmosphere was added to each frame to evaluate the algorithm under the most severe conditions.

3.2.1 Optimization parameters

Number of modes controlled and optimization time

The test with only the optimization algorithm to control the mirror shape according to the image metric showed decent results but required significant tuning to the algorithm. The first issue was a number of controlled modes. It was expected that a low number of modes would be sufficient to correct the mirror surface, but that was not the case. To find the optimum number of modes to control for the algorithm multiple tests were done with adjustments to the simplex size and an increase in optimization time. The figure Figure 3.8a and Figure 3.8b, have identical optimization settings except for the number of the modes controlled and slightly smaller simplex size. Although the results for the cost value and IDD radius (radius in the title of PSF figure) are very similar for both cases, there is a significant difference in the convergence. Even with larger simplex the convergence while controlling 5 modes is rapid compared to the case of 49 modes control, and does not indicate of any change over the rest of the optimization. Even if the number of allowed cost function evaluation would be increased the result would not improve. Whereas when controlling 49 modes the convergence is much slower due to the expanded search space, but with a promise of better result since the converges did not settle even after 1200 iterations.

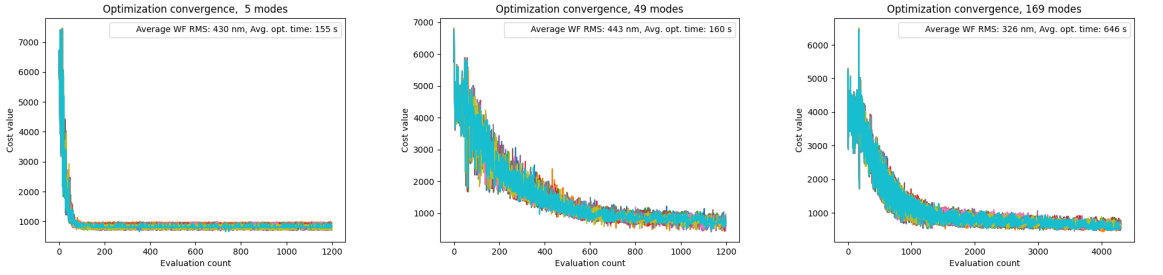

(a) 5 mode control convergence (b) 49 mode control convergence (c) 169 mode control convergence

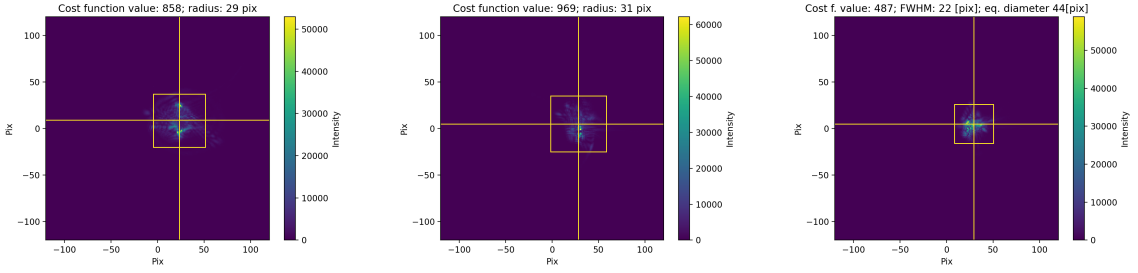

(d) Optimized PSF, 5 modes (e) Optimized PSF, 49 modes (f) Optimized PSF, 169 modes

Figure 3.8: Optimization convergence and final PSF frame of 1st trial for a different number of controlled Zernike modes. The 5 and 49 mode function evaluation limit is 1200 whereas 169 control was 4300. The simplex is smaller for an increased number of modes. Intensity is measured in pixel well bits.

This indicated that controlling modes might enable the system to achieve lower cost values and better PSF. Due to this reason, it was decided to increase not only the number of controlled modes but also the maximum optimization time to the maximum of 10 minutes and examine the best possible convergence. The Figure 3.8c shows the result while controlling 169 modes where the convergence does not stop decreasing and is capable of achieving good results. If it was terminated at the same function evaluation count as the other two experiments, it would have a similar result. Therefore a combination of a large number of modes to control and enough time to allow for convergence is required to achieve a good result.

The convergence figures contain a legend entry stating the average optimization time for all 10 iterations as well as an average of computed and actuated wavefront displacement in nm RMS. This is not the measurement of the wavefront, but an estimation of the wavefront constructed for the control of the mirror.

Optimization convergence sensitivity to simplex size

The importance of the initial guess for the optimization algorithm was shown to be decisive. This was confirmed in the test setting while controlling 151 modes, and otherwise identical settings except for the simplex size. The Figure 3.9 presents the result from 3 simplex coordinate guesses of $0.1, 0.3$, and $0.6\mu m$. Notably, the coefficients are smaller than the simplex of $1\mu m$ in the modeled optimization. This might be due to the actuator displacement/current conversion ratio being too large as it was only an estimate from the datasheet.

The expected result was found with the smallest simplex size with slow and incomplete convergence. The simplex of $0.3\mu m$ had better performance but was unable to converge to an acceptable result. The largest simplex size had the worst performance with an identically unstable convergence for all 10 trials. This behavior was not observed in the model and could be a result of a mismatch between the control conversion ratio and between actuated and modeled Zernike modes. Therefore the simplex for all the testing was chosen to be at $0.5\mu m$, as it showed the best performance and most stable convergence.

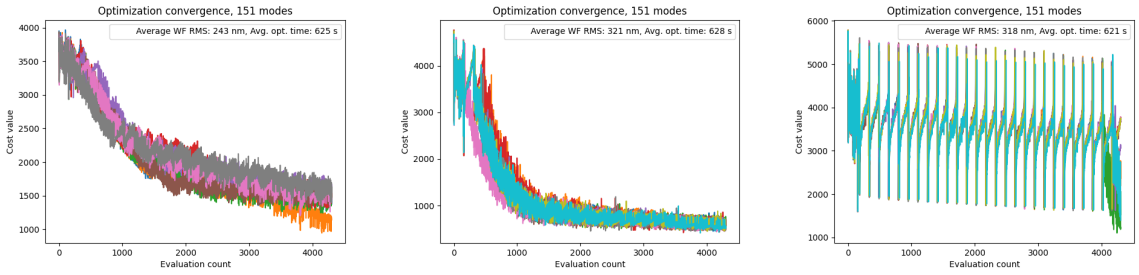

(a) Simplex $0.1\mu m$ (b) Simplex $0.3\mu m$ (c) Simplex $0.6\mu m$

Figure 3.9: Image metric optimization controlling 151 modes with different initial simplex size. ROI 240×240 pixels, 4300 function evaluation limit.

Initial mirror error

The optimization trials for the modeled system were done with different mirror errors, whereas in the test case, each trial had attempted to optimize the same mirror error. The initial unactuated mirror error is presented in Figure 3.10, where the intensity is measured in bits. The FWHM is measured by evaluating the square area containing half of the maximum intensity values thus for initial error PSF is not valuable. The eq. diameter indicates IDD box width which is much more useful when comparing the performance of severely deformed PSF. The center of the PSF is slightly decentered and will remain such, to leave some space for sampling the top left corner completely dark for the filtering calculation.

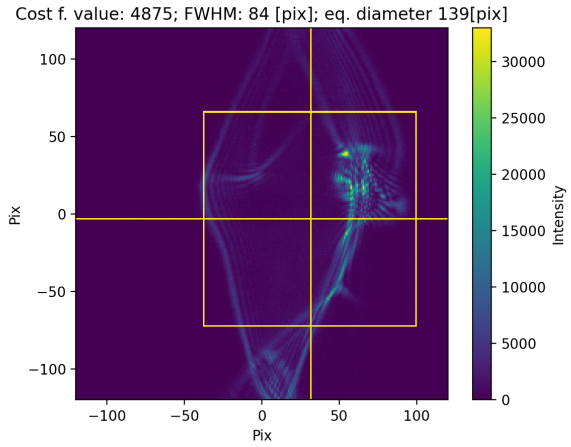

Figure 3.10: The initial PSF with mirror actuators at rest.

3.2.2 Result without the atmospheric aberration

Using the previously mentioned parameters for the simplex, function evaluation count, ROI, and camera image filtering the method was capable of converging to a comparable result with the modeled system. Although the optimization was allowed to run for until the time limit of 10 minutes to achieve the results. The convergence over the iterations is very similar to the modeled case and is presented in Figure 3.11. In the beginning, the convergence is quick due to the change in PSF being much more noticeable. As it gets closer to the ideal PSF the metric loses its capability to distinguish the change in wavefront thus the convergence becomes very slow. The large number of modes controlled results in a slow, but much more capable flattening method. The average displacement of the WF nm RMS of 10 trials is only the value of the computed final wavefront for the control signal. Due to the actuator current conversion ratio being inaccurate the actual WF displacement RMS will be at least twice as big.

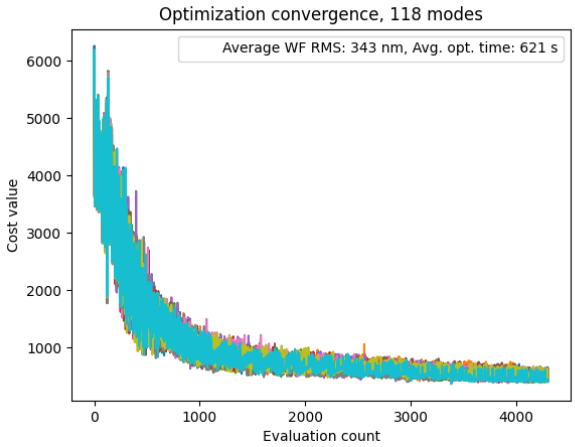

Figure 3.11: The optimization convergence of flattening method using 118 control modes, ROI 240×240 pixels, exposure 0.9 s, simplex 0.5μm

The initial PSF is larger and worse than the unactuated mirror as can be seen in Figure 3.12 due to the simplex initial guess actuating the defocus mode. Both initial PSFs are the same, due to all trials not having randomly generated simulated mirror errors as in the model. The optimized PSF of the 1st and 5th attempts are shown below, with an average FWHM of 20 pix and a DDI width of 40 pix. The pixels here are binned in 2 × 2 boxes, thus they have a size of 6.9μm. The algorithm was not capable of converging to an ideal PSF shape of a few pixels.

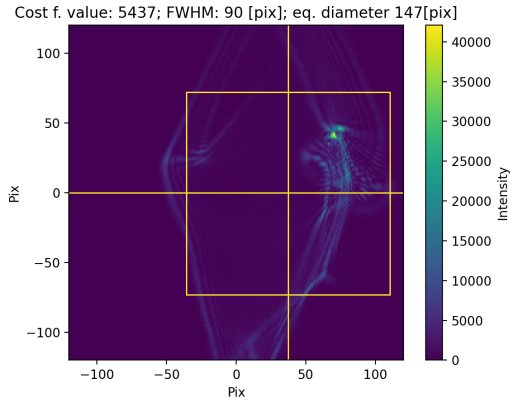

(a) Trial 1 initial frame

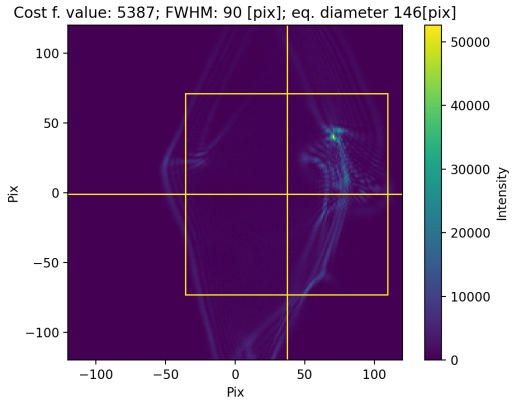

(b) Trial 5 initial frame

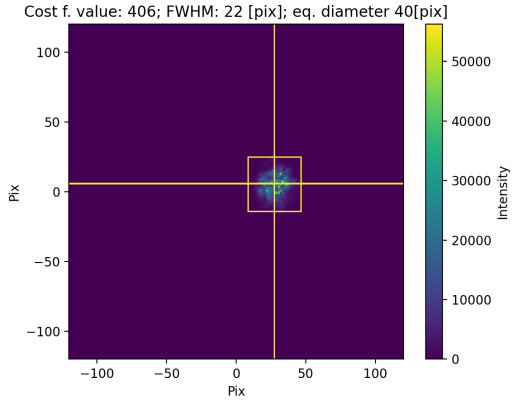

(c) Trial 1 final frame

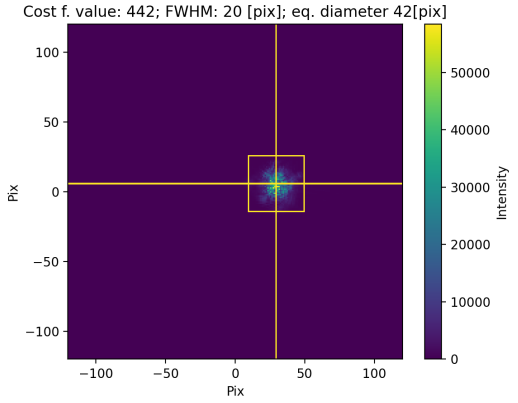

(d) Trial 5 final frame

Figure 3.12: Initial and final frames of 1st and 5th trial from optimization controlling 118 modes. The simplex size 0.6μm, exposure 0.9 s, function evaluation limit 4300, ROI 240 $\times$ 240. Intensity is measured in bits.

3.2.3 Simulated atmospheric aberrations

To fully answer the research question of whether the flattening algorithm can flatten the mirror using a natural guide star, atmospheric aberration has to be added to the test. This is also required to reasonably compare the result between the model and the test since the model optimization was performed with the atmosphere. The physical simulation of atmospheric aberrations in a controlled and well-determined manner requires significant resources and time. An easier computational option is available in which a simulated observed PSF with ideal optics and atmospheric aberrations is convolved with the true observed PSF. A modeled example of such observed PSF with ideal optics, but with atmospheric aberrations is presented in the Figure 3.13 which has a Gaussian profile. This Gaussian profile can be convolved with the PSF image seen in the previous result to induce atmospheric aberrations. This is possible because each point source being imaged due to aberrations would be blurred in the shape of such Gaussian. It can be assumed that each pixel is then a point that takes upon the shape of Gaussian aberration. Then it acts as a sort of blurring filter simulating the aberrations.

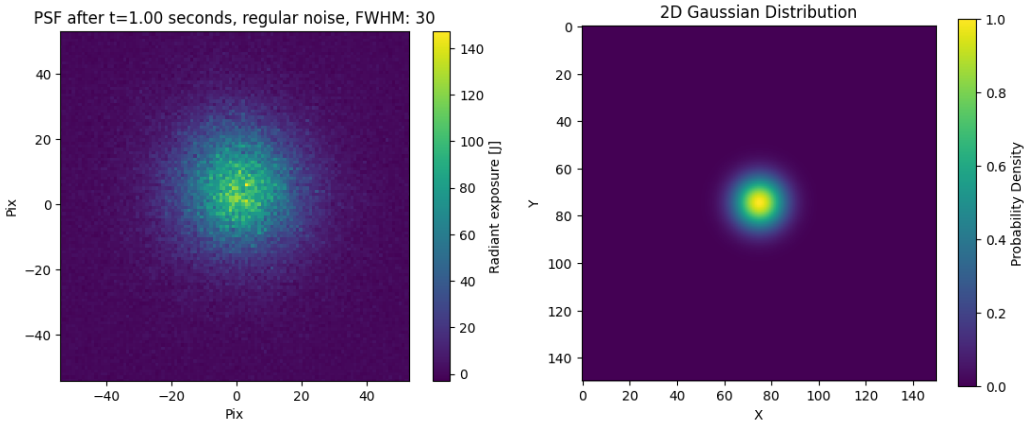

(a) Modeled multi-layer Mauna Kea atmosphere (b) Approximated aberration

Figure 3.13: Gaussian distribution of PSF due to atmospheric aberrations in case of ideal optics. Modeled and approximated atmosphere of Mauna Kea

The figure on the left is with modeled atmosphere for Mauna Kea with an FWHM of 30 pixels or 0.9 arcseconds after converting with the pixel scale ratio of 0.03. Using the Equation 3.2[30] Fried parameter is 13.2 which is considered the worst seeing[31]. The modeled atmosphere is worse than what is typically found at Mauna Kea most likely due to the multiple layers being used. The typical fried parameter r_0 at Mauna Kea is 20 cm [31] and using the Equation 3.2 it can be converted to 0.6 arcseconds. Using the pixel scale it is converted to roughly 20 pixels on the camera. The figure on the right is modeled Gaussian distribution with seeing of 20 pixels. The test case was modeled with the approximated aberration.

$$\theta_{FWHM} = 2.013\text{e}5\frac{\lambda}{r_0} \tag{3.2}$$

The example of the convolution is presented in Figure 3.14, where a single line with increasing intensity is convolved with the PSF which is aberrated with approximated Gaussian. This results in the line being blurred and the difference in the intensity remains due to the Gaussian being 1 at maximum. This operation is then performed between each frame capture of plain PSF and before sending the frame for the image metric evaluation. This effectively simulates the aberration for the test of the flattening method without relying on phase plates. The downside is longer testing time due to computational load, but the convolution time is subtracted from the timing of the optimization.

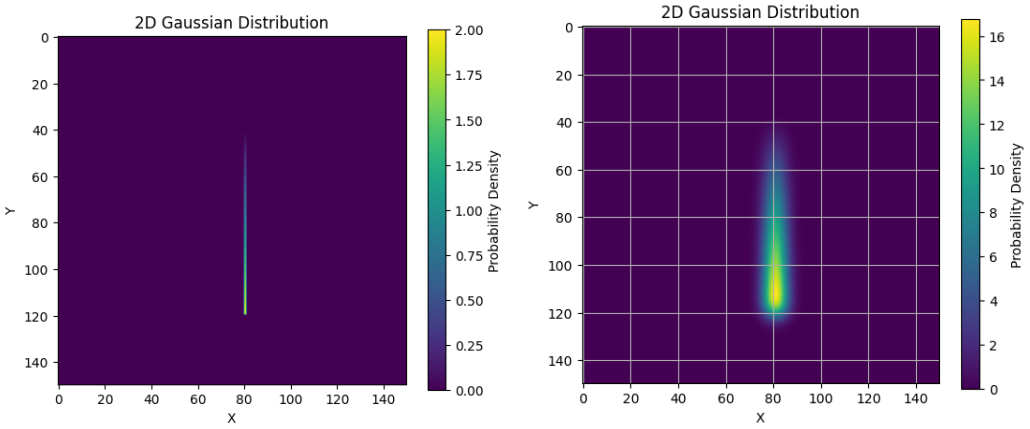

(a) Single pixel line with increasing intensity (b) A line convolved with the aberration

Figure 3.14: Convolution of line with the approximated atmospheric aberration PSF

3.2.4 Results with approximated aberration

With the atmospheric aberrations implemented in the test, it is now possible to fully answer the research question and gauge the capability of the method. The test to provide an answer was carried out with the same

optimization setting without the aberration. The slight difference is that one batch of trials was cut at the 5-minute mark and the other was left to run for a maximum limit of 10 minutes. This was done to evaluate if the algorithm could be stopped sooner. The final results were comparable to the modeled flattening case with slightly better results according to the image metric, thus suggesting that the mirror was capable of achieving a similar surface error of at least 100 nm.

The addition of aberration slightly differs from the flattening without them as each image passed to the image metric is now not as sharp. The comparison example presented in Figure 3.15, shows mirror PSF with the simulated aberration and without for initial optimization frame with simplex of $0.5\mu m$. The image metric cost and equivalent diameter of IDD are slightly smaller due to the smoothing of the image metric.

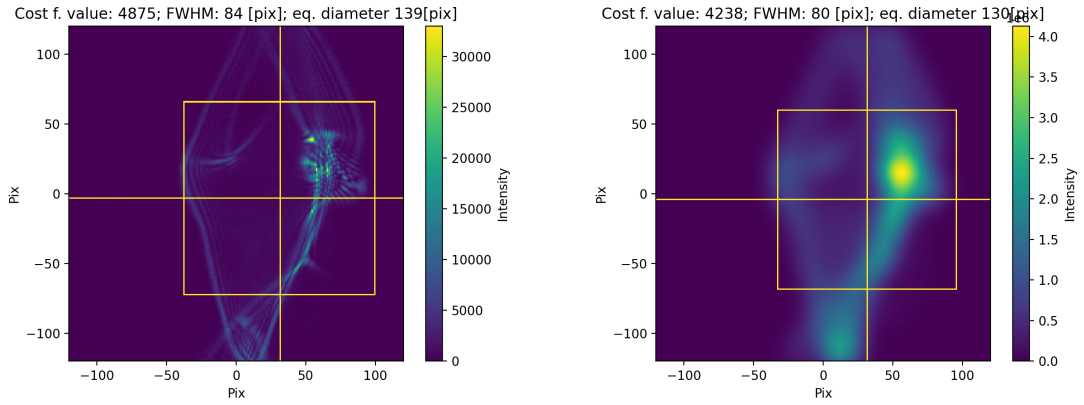

(a) Without aberration

(b) With aberration

Figure 3.15: A PSF convolved with approximated atmospheric Gaussian distribution signal

The optimization convergence profile shown inFigure 3.16, was identical to the optimization without the aberration, but slightly more defined with more smoothness after roughly 1000 evaluations. It indicated better results than the plain flattening clearly due to the decreased image metric sensitivity to actuated mode. This is due to the simulated aberration providing signal conditioning and smoothing the error between actuated and simulated modes. As expected the increase in optimization time did not change the result in any significant way.

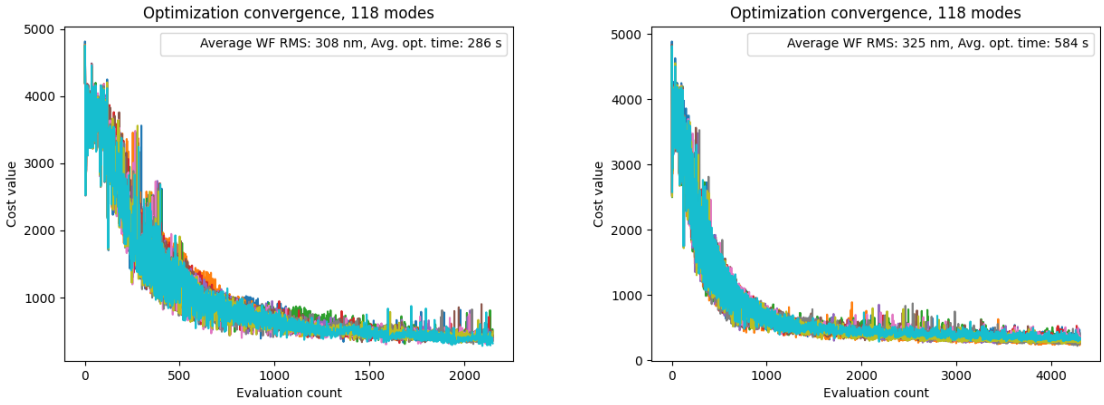

(a) 5 min convergence

(b) 10 min convergence

Figure 3.16: The optimization convergence of flattening with simulated aberrations using 118 control modes, ROI 240×240 pixels, exposure 0.9 s, simplex $0.5\mu m$. Function evaluation limit set to 2300

The final results were comparable both to the modeled case and test without the aberrations. Comparing optimized PSF test results with and without aberration, it seemed that the flattened mirror PSF from the test with the simulated aberration was able to achieve similar results much more consistently. Although the FWHM in both tests are very similar with 22 pixels on average for 10 trials. Thus the aberration improved only the

consistency at reaching similar flatness. The 5-minute optimization was able to yield just slightly fewer results with an average FWHM of 24 pixels, which is still slightly better than the modeled case.

The flattened mirror PSF with the aberration had better results compared to the model case when comparing the equivalent diameter and cost value. The average IDD of optimized PSF for the modeled case was 39 pixels and 34 pixels for the test case. The final PSF FWHM for 5 min optimization was on average 5 pixels larger than the FWHM of the ideal Gaussian aberration, and for 10 min optimization with much less improvement by 4 pixels.

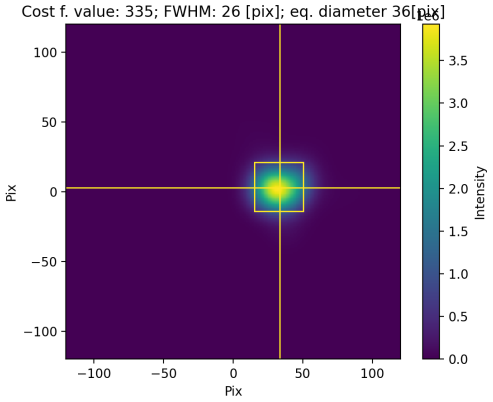

(a) Final frame of 5 min opt.

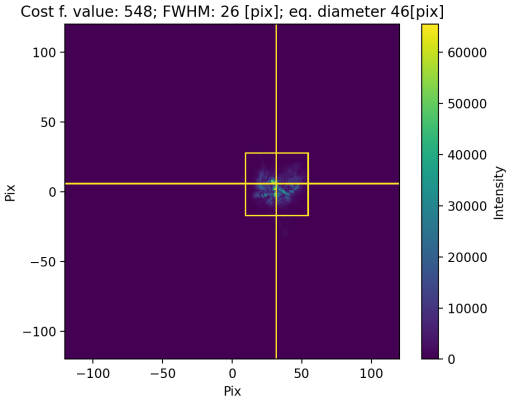

(b) Final frame of 5 min opt. without aberration

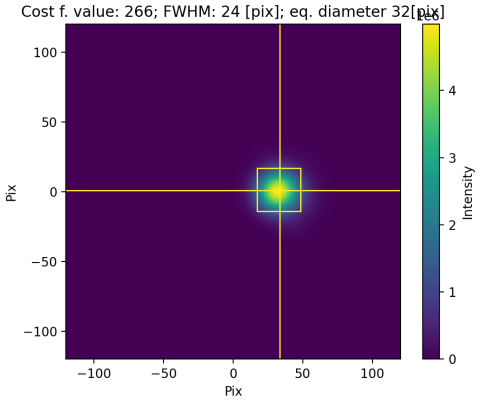

(c) Final frame of 10 min opt.

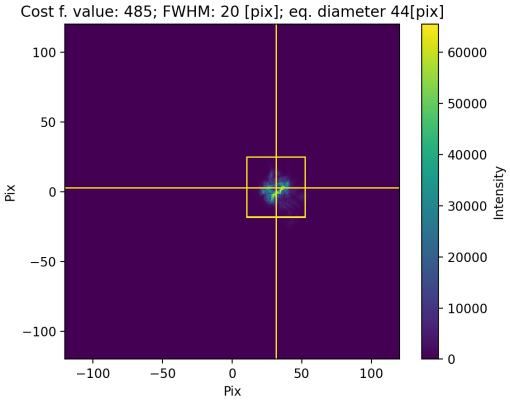

(d) Final frame of 10 min opt. without aberration

Figure 3.17: Initial and final frames of 1st and 5th trial from optimization controlling 118 modes. The simplex size 0.5μm, exposure 0.9 s, function evaluation limit 4300, ROI 240 $\times$ 240. Intensity is measured in bits.

Conclusion

The research topic posed the question if the UH-88 convex adaptive secondary mirror, being developed by TNO, can be flattened to act as a passive mirror using only a natural star as a light source and a focal plane camera as a measurement device. The flattening under such conditions is required since it is assumed that the wavefront sensor is not available and the calibrated commands for flattening are out of date. To answer the question numerical model was coded which followed predetermined requirements allowing the model and UH-88 system to be equivalent for evaluating the model. To verify whether the model is realistic and the method plausible solution for the UH-88 a test having the critical of the model components was built in the laboratory.

The research question after requirement formulation was expanded into specific conditions that the flattening method has to satisfy. The conditions were mirror flatness, low-light distorted light, and time limit. For the ASM to become passive it is required to have a surface error of 100 nm RMS. The low light was assumed to be the brightest star with $0.14mW$ at the focal plane and was distorted by Mauna Kea's atmosphere. The time limit for the flattening procedure was 10 minutes.

The model contained all the critical components to resemble the UH-88 system. The natural star with its predefined power which is then propagated through the multi-layer Mauna Kea atmosphere. To save computational time the light was modeled as a single wavelength wavefront of 590 nm. This can be done because the relative spread of wide-band light is lower than the aberration smearing over long exposure. The deformable mirror control with the simulated expected surface error of $12\mu m$ PV. And finally a focal plane camera with the same pixel size as EMCCD and similar low noise.

The flattening method was based on the focal plane image metric and direct search optimization algorithm. In the modeled case it controlled the mirror with a linear combination of 10 Zernike modes, excluding piston and tip/tilt modes. The modeled mirror error was generated also by 10 modes which allowed to perfectly correct those modes, without modeling error between theoretical and actuated Zernike modes. This error was not expected to be large therefore it was not modeled to save time. The final result was promising, with 1 minute optimization the mirror surface was on average 93 nm RMS, which is slightly better than the expected 100 nm RMS. The optimization was terminated by cost function tolerance and not the function evaluation limit. This suggests that with a smaller tolerance, it could have achieved even better results.

The test setup intended to replicate the result was built using DM developed by TNO which has the same actuator architecture as the ASM of UH-88. The evaluation of the optics for connecting the light source, DM, and the camera was shown to have roughly 54 nm RMS error from the Roddier test, This error should not be visible and could be well hidden within the PSF. Nevertheless, the test setup was not a perfect replica, since the light source was set to be much stronger to compensate for the strong noise of the CMOS camera. Due to the high noise of the camera, additional high-pass filtering was required to improve the performance of the image metric. Additionally, it was not possible to achieve good flattening results by controlling 10 Zernike modes. It required controlling 118 modes for the best result as well as running the optimization for the maximum time limit of 10 minutes. This large difference with the model is most likely due to the error between theoretical and actuated modes. This could be attributed to the actuator layout and noisy camera. The other issue was that there was no readily available way of simulating the physical atmosphere in the lab with the phase plates. Therefore an ideal aberration approximation was used to convolve with the PSF image, effectively blurring them like a real atmosphere would do.

Nevertheless, the test results were still promising and slightly better than the model. Unfortunately, the mirror surface cannot be measured directly for the test, but because within the numerical model, the wavefront of the mirror is known, it is possible to use it for comparison. The average equivalent width of the optimized PSF was 40 pixels with the aberration and had the wavefront error of 93 nm RMS. The test case with aberration showed the average width of the final PSF was 36 pix after 5 minutes of optimization, and only 6 pixels wider than the Gaussian shape aberration with perfect optics. This indicates that the mirror could have been close to the 100 nm RMS surface error or even better as the model had a larger final PSF. The 10-minute optimization showed PSF of 24 pix FWHM and 32 pix in equivalent diameter which is almost a quarter better than the

modeled final mirror surface error and only 4 pixels larger than the perfect aberrations Gaussian FWHM.

In the end, both the model and the test results of the flattening method showed that the image metric-based optimization controlling the mirror was able to converge to a good mirror surface error, close to 100 nm RMS, and within 10 minutes with low light conditions and atmospheric aberrations. However further modeling and testing improvements are necessary to make the method more certain and robust. A better model of the system would allow to use faster optimization algorithm that would rely on precise and smooth cost function response. Further testing with a low-noise camera and better-matched power for the light source would improve the understanding and bring it closer to implementation.

Appendix A

Image metric

The further mathematical method describes how the image metric is calculated for each image frame. Define x and y arrays as linear ranges for the dimensions of the image IM:

$$x_{\text{arr}} = \{0, 1, 2, \ldots, N_x - 1\}, \quad y_{\text{arr}} = \{0, 1, 2, \ldots, N_y - 1\}$$

where $N_x = \text{im.shape}[0]$ and $N_y = \text{im.shape}[1]$.

The total intensity is computed as:

$$\text{tot} = \sum_{i=0}^{N_x-1} \sum_{j=0}^{N_y-1} \text{im}[i, j]$$

Calculate the center of mass coordinates x_{cm} and y_{cm} as follows:

$$y_{\text{cm}} = \frac{\sum_{j=0}^{N_y-1} \left(\sum_{i=0}^{N_x-1} \text{im}[i, j] \right) \cdot y_{\text{arr}}[j]}{\text{tot}}$$

$$x_{\text{cm}} = \frac{\sum_{i=0}^{N_x-1} \left(\sum_{j=0}^{N_y-1} \text{im}[i, j] \right) \cdot x_{\text{arr}}[i]}{\text{tot}}$$

Shift and square each array relative to the center of mass point:

$$x_{\text{arr}} = (x_{\text{arr}} - x_{\text{cm}})^2$$

$$y_{\text{arr}} = (y_{\text{arr}} - y_{\text{cm}})^2$$

Given:

$$x_{\text{arr}} = \left[x_0^2, x_1^2, x_2^2, \ldots, x_{N_x-1}^2 \right]$$

$$y_{\text{arr}} = \left[y_0^2, y_1^2, y_2^2, \ldots, y_{N_y-1}^2 \right]$$

where x_i^2 and y_j^2 are the squared distances along the x-axis and y-axis respectively.

The squared radial distance matrix r^2 is constructed as:

$$r^2 = \begin{bmatrix} x_0^2 + y_0^2 & x_0^2 + y_1^2 & \cdots & x_0^2 + y_{N_y-1}^2 \\ x_1^2 + y_0^2 & x_1^2 + y_1^2 & \cdots & x_1^2 + y_{N_y-1}^2 \\ \vdots & \vdots & \ddots & \vdots \\ x_{N_x-1}^2 + y_0^2 & x_{N_x-1}^2 + y_1^2 & \cdots & x_{N_x-1}^2 + y_{N_y-1}^2 \end{bmatrix}$$

Each entry r_{ij}^2 in the matrix is calculated as:

$$r_{ij}^2 = x_i^2 + y_j^2$$

where $i = 0, 1, \ldots, N_x - 1$ and $j = 0, 1, \ldots, N_y - 1$.

Thus, r^2 is a 2D matrix of shape (N_x, N_y), where each element represents the squared radial distance from a reference origin for a given point (i, j).

Compute the moment of inertia (MoI) of the image:

$$\text{MoI} = \sum_{i=0}^{N_x-1} \sum_{j=0}^{N_y-1} r^2[i, j] \cdot \text{im}[i, j]$$

Finally, calculate the image metric cost c as:

$$c = \frac{\text{MoI}}{\sum_{i=0}^{N_x-1} \sum_{j=0}^{N_y-1} \text{im}[i,j]}$$

Atmosphere and Noise with deformed mirror

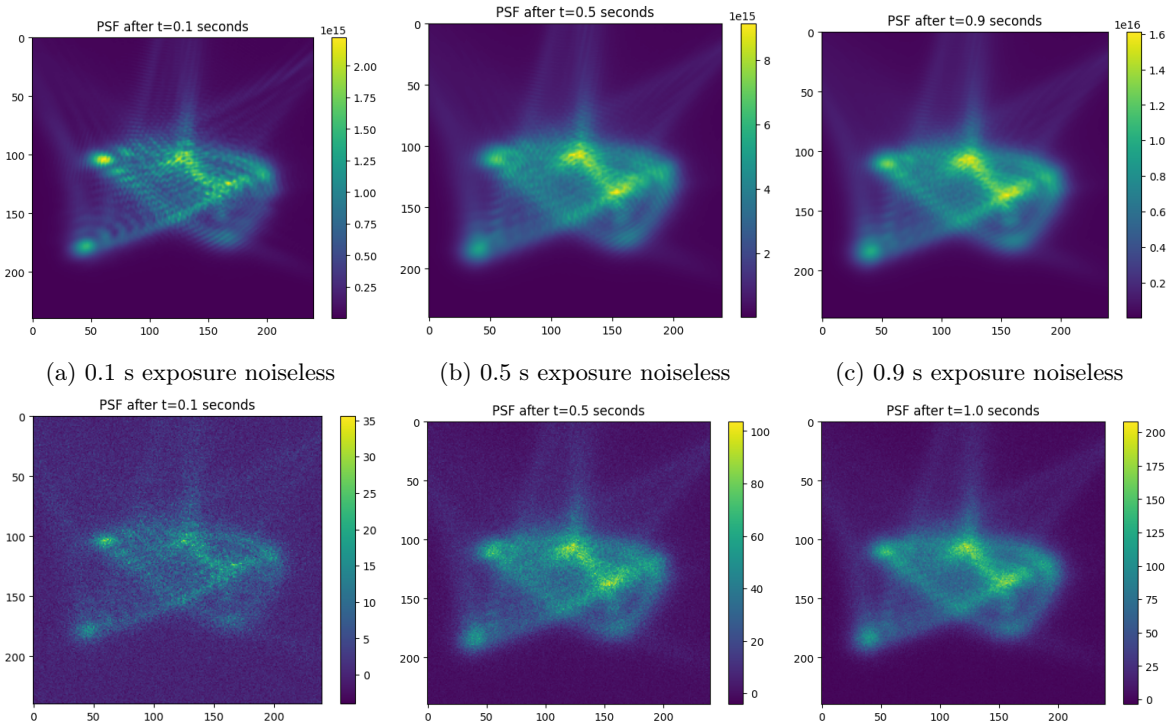

(a) 0.1 s exposure noiseless (b) 0.5 s exposure noiseless (c) 0.9 s exposure noiseless

(d) 0.1 s exposure with noise (e) 0.5 s exposure with noise (f) 1 s exposure with noise

Figure 3.18: The PSF with Mauna Kea atmospheric aberrations for different exposure times. The top row does not include camera noise, whereas the bottom has noise.

Model optimization result with different parameters and noise

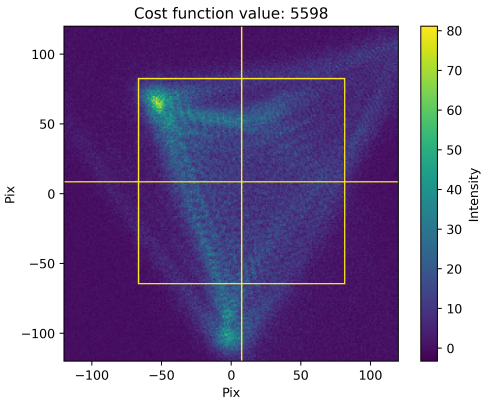

(a) Trial 1 initial frame

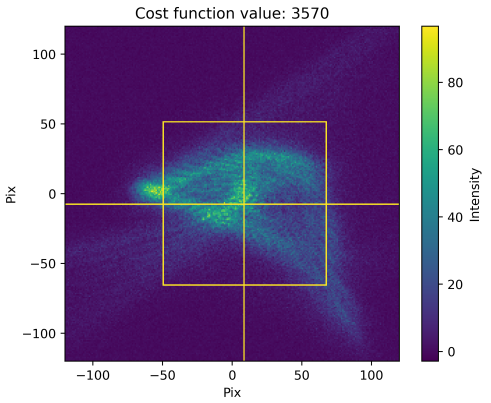

(b) Trial 5 initial frame

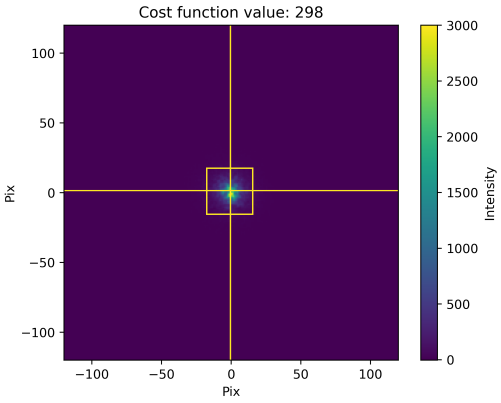

(c) Trial 1 final frame, remaining WFE 51 nm RMS

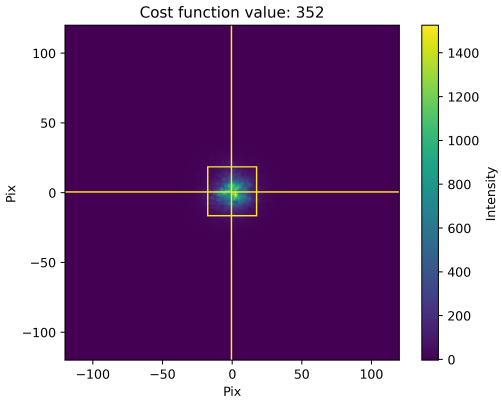

(d) Trial 5 final frame, remaining WFE 119 nm RMS

Figure 3.19: Trial 1 and 5 initial and final frames from the optimization process. The exposure time for all trials is $0.1s$.

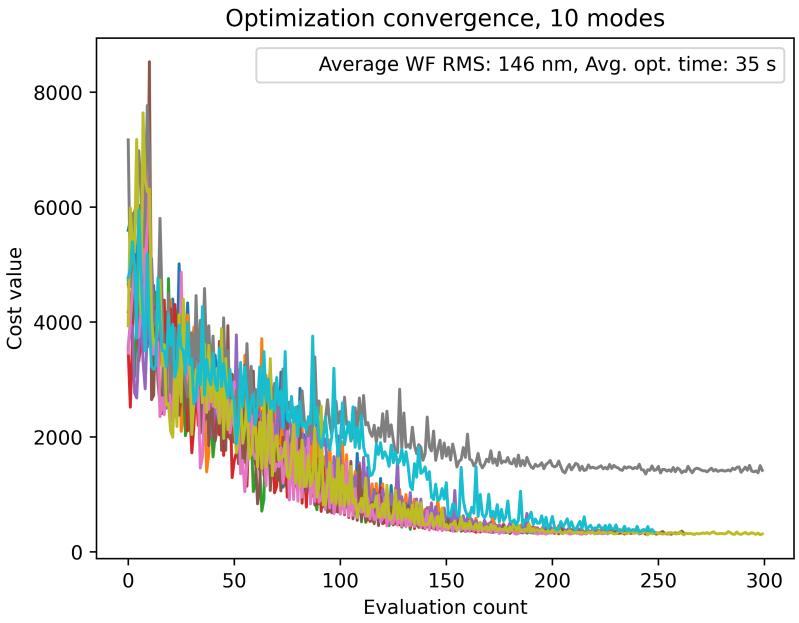

Figure 3.20: Caption

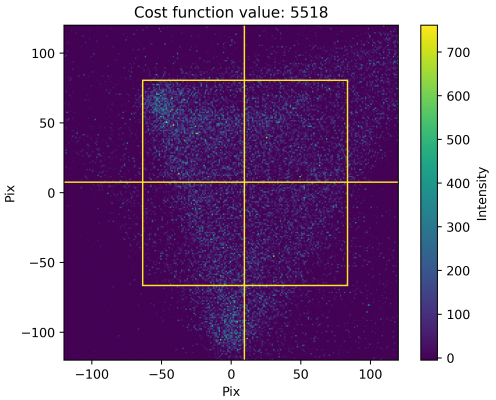

(a) Trial 1 initial frame

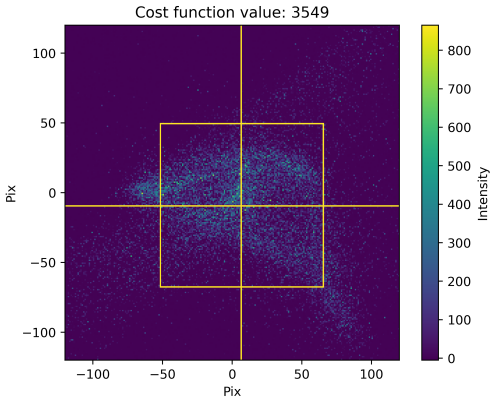

(b) Trial 5 initial frame

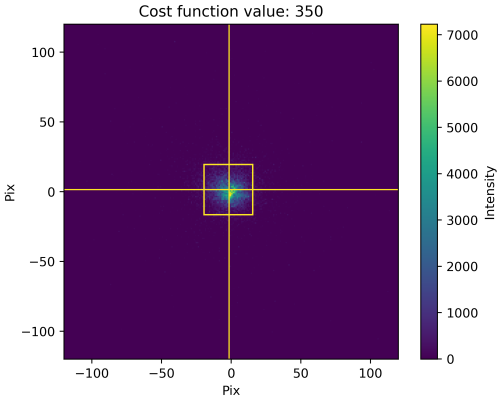

(c) Trial 1 final frame, remaining WFE 51 nm RMS

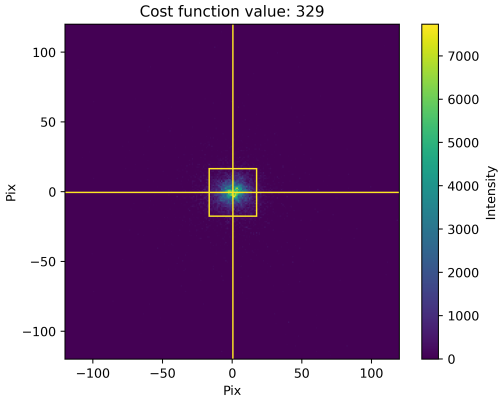

(d) Trial 5 final frame, remaining WFE 119 nm RMS

Figure 3.21: Trial 1 and 5 initial and final frames from the optimization process with EMCCD noise and gain of 50. The exposure time for all trials is $1ms$.

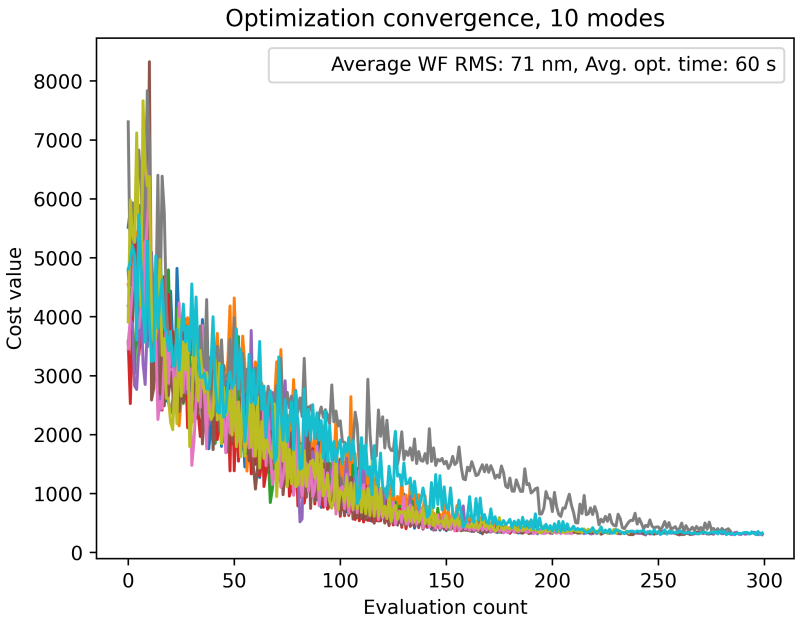

Figure 3.22: Caption

The project code and flattening animations can be found in GitHub Repository.

References

[1] *Calibration and Testing of the 6.5 M MMT Adaptive Optics System*. URL: https://apps.dtic.mil/sti/citations/tr/ADA393583.

[2] Stefan Kuiper et al. *UH2.2 Adaptive Secondary Mirror Development*. Tech. rep.

[3] Rachel Bowens-Rubin et al. "Performance of Large-Format Deformable Mirrors Constructed with TNO Variable Reluctance Actuators". In: ().

[4] Mazen M. Sinjab and Arthur B. Cummings. "Introduction to wavefront science". In: *Customized Laser Vision Correction* (June 2018), pp. 65–94. DOI: 10.1007/978-3-319-72263-4{_}2/FIGURES/21. URL: https://link-springer-com.tudelft.idm.oclc.org/chapter/10.1007/978-3-319-72263-4_2.

[5] *(PDF) Implementation of Branch-Point-Tolerant Wavefront Reconstructor for Strong Turbulence Compensation*. URL: https://www.researchgate.net/publication/277761247_Implementation_of_Branch-Point-Tolerant_Wavefront_Reconstructor_for_Strong_Turbulence_Compensation.

[6] Jacopo Antonello et al. *Semidefinite programming for model-based sensorless adaptive optics*. Tech. rep. 2012.

[7] Guchuan Zhu et al. "Flatness-based control of electrostatically actuated MEMS with application to adaptive optics: A simulation study". In: *Journal of Microelectromechanical Systems* 15.5 (Oct. 2006), pp. 1165–1174. ISSN: 10577157. DOI: 10.1109/JMEMS.2006.880198. URL: https://www.researchgate.net/publication/44284956_Flatness-Based_Control_of_Electrostatically_Actuated_MEMS_With_Application_to_Adaptive_Optics_A_Simulation_Study.

[8] Vyas Akondi and Alfredo Dubra. "Shack-Hartmann wavefront sensor optical dynamic range". In: *Optics Express* 29.6 (Mar. 2021), p. 8417. ISSN: 10944087. DOI: 10.1364/OE.419311. URL: /pmc/articles/PMC8237929/%20/pmc/articles/PMC8237929/?report=abstract%20https://www.ncbi.nlm.nih.gov/pmc/articles/PMC8237929/.

[9] Runa Briguglio et al. "Optical calibration and performance of the adaptive secondary mirror at the Magellan telescope". In: *Scientific Reports 2018 8:1* 8.1 (July 2018), pp. 1–12. ISSN: 2045-2322. DOI: 10.1038/s41598-018-29171-6. URL: https://www.nature.com/articles/s41598-018-29171-6.

[10] Johann Kolb, Kolb, and Johann. "Review of AO calibrations, or how to best educate your AO system". In: *SPIE* 9909 (July 2016), 99090K. ISSN: 0277-786X. DOI: 10.1117/12.2232874. URL: https://ui.adsabs.harvard.edu/abs/2016SPIE.9909E..0KK/abstract.

[11] Emiel H. Por et al. "High Contrast Imaging for Python (HCIPy): an open-source adaptive optics and coronagraph simulator". In: (July 2018), p. 152. ISSN: 1996756X. DOI: 10.1117/12.2314407.

[12] Wouter Jonker et al. *Hot forming of a large deformable mirror facesheet*. Tech. rep. DOI: 10.1117/12.2629810. URL: https://www.spiedigitallibrary.org/conference-proceedings-of-spie/12188/121880S/Hot-forming-of-a-large-deformable-mirror-facesheet/10.1117/12.2629810.full.

[13] Christoph Baranec et al. "The Robo-AO-2 facility for rapid visible/near-infrared AO imaging and the demonstration of hybrid techniques". In: (June 2018). URL: https://arxiv.org/abs/1806.01957v1.

[14] Stefan Kuiper et al. "Advances of TNO's electromagnetic deformable mirror development". In: *https://doi-org.tudelft.idm.oclc.org/10.1117/12.2311981* 10706 (July 2018), pp. 345–352. ISSN: 1996756X. DOI: 10.1117/12.2311981. URL: https://www-spiedigitallibrary-org.tudelft.idm.oclc.org/conference-proceedings-of-spie/10706/1070619/Advances-of-TNOs-electromagnetic-deformable-mirror-development/10.1117/12.2311981.full%20https://www-spiedigitallibrary-org.tudelft.idm.oclc.org/conference-proceedings-of-spie/10706/1070619/Advances-of-TNOs-electromagnetic-deformable-mirror-development/10.1117/12.2311981.short.

[15] Rachel Bowens-Rubin et al. "Performance of Large-Format Deformable Mirrors Constructed with Hybrid Variable Reluctance Actuators II: Initial Lab Results from FLASH". In: (Oct. 2021). DOI: 10.1117/12.2593535. URL: https://www.researchgate.net/publication/355093073_Performance_of_Large-Format_Deformable_Mirrors_Constructed_with_Hybrid_Variable_Reluctance_Actuators_II_Initial_Lab_Results_from_FLASH%20http://dx.doi.org/10.1117/12.2593535.

[16] Stefan Kuiper et al. *Adaptive Secondary Mirror development for the UH-88 telescope*. Tech. rep. URL: https://hal.science/hal-02384381.

[17] *Signal and Noises*. URL: https://www.eso.org/~ohainaut/ccd/sn.html.

[18] *iXon Ultra 888 EMCCD - Andor - Oxford Instruments*. URL: https://andor.oxinst.com/products/ixon-emccd-camera-series/ixon-ultra-888#product-information-tabs.

[19] Max Born et al. "Principles of Optics: Electromagnetic Theory of Propagation, Interference and Diffraction of Light". In: *Principles of Optics* (Oct. 1999). DOI: 10.1017/CBO9781139644181. URL: https://www-cambridge-org.tudelft.idm.oclc.org/core/books/principles-of-optics/D12868B8AE26B83D6D3C2193E94FFC3

[20] James. Binney and Michael. Merrifield. "Galactic Astronomy James Binney, Michael Merrifield". In: (2021), p. 816.

[21] *Atlas 12.3 MP Model (Sony IMX253) - 5GigE Camera*. URL: https://thinklucid.com/product/atlas-12-mp-imx253/.

[22] R. C. Ramsey. "Spectral Irradiance from Stars and Planets, above the Atmosphere, from 0.1 to 100.0 Microns". In: *Applied Optics, Vol. 1, Issue 4, pp. 465-471* 1.4 (July 1962), pp. 465–471. ISSN: 2155-3165. DOI: 10.1364/AO.1.000465. URL: https://opg.optica.org/viewmedia.cfm?uri=ao-1-4-465&seq=0&html=true%20https://opg.optica.org/abstract.cfm?uri=ao-1-4-465%20https://opg.optica.org/ao/abstract.cfm?uri=ao-1-4-465.

[23] *Commercial telescopes*. URL: https://www.telescope-optics.net/commercial_telescopes.htm#zones.

[24] Christopher Neyman. "Atmospheric Parameters for Mauna Kea". In: (2004). URL: http://www.naoj.org/Observing/Telescope/Image/seeing.html.

[25] *Fourier Optics and the Complex Pupil Function | Strolls with my Dog*. URL: https://www.strollswithmydog.com/fourier-optics-complex-pupil-function/.

[26] J W Goodman. "Introduction to Fourier Optics, 3rd". In: *Quantum and Semiclassical Optics: Journal of the European Optical Society Part B* (2005), p. 491. URL: https://books.google.com/books/about/Introduction_to_Fourier_Optics.html?id=QllRAAAAMAAJ.

[27] *Lecture notes April 2017 - SC42030 Control for High Resolution Imaging (2022/23 Q4)*. URL: https://brightspace.tudelft.nl/d2l/le/content/500986/viewContent/2936479/View.

[28] Matthias Schöck et al. "Atmospheric turbulence characterization with the Keck adaptive optics systems. I. Open-loop data". In: *Applied Optics, Vol. 42, Issue 19, pp. 3705-3720* 42.19 (July 2003), pp. 3705–3720. ISSN: 2155-3165. DOI: 10.1364/AO.42.003705. URL: https://opg.optica.org/viewmedia.cfm?uri=ao-42-19-3705&seq=0&html=true%20https://opg.optica.org/abstract.cfm?uri=ao-42-19-3705%20https://opg.optica.org/ao/abstract.cfm?uri=ao-42-19-3705.

[29] *Thorlabs wavefront specifications*. URL: https://www.thorlabs.com/catalogpages/V21/1613.pdf.

[30] *Seeing*. URL: https://www.eso.org/gen-fac/pubs/astclim/papers/lz-thesis/node11.html#F_r0.

[31] Christopher Neyman. "Atmospheric Parameters for Mauna Kea". In: (2004). URL: http://www.naoj.org/Observing/Telescope/Image/seeing.html.